Journal of Computational Physics (2019)

Contents lists available at ScienceDirect

Journal of Computational Physics

journal homepage: www.elsevier.com/locate/jcp

Discontinuous Galerkin methods for multi-layer ocean modeling: viscosity and thin layers

Robert L. Higdon

Department of Mathematics, Oregon State University, Corvallis, Oregon 97331-4605, United States

ARTICLE INFO

Article history:
Accepted October 6, 2019

2000 MSC: 65M99, 86A05

Keywords: multi-layer ocean models, discontinuous Galerkin

ABSTRACT

The work described here is part of a continuing project to develop, analyze, and test some procedures for using discontinuous Galerkin (DG) numerical methods in multi-layer, isopycnic models of ocean circulation. The steps taken in the present paper include the following.

(1) Develop an implementation of horizontal viscosity for usage in DG methods for multi-layer models. This step involves a formulation of the local DG method that can be used in the context of barotropic-baroclinic splitting, a widely-used approach to handling the multiple time scales in ocean circulation models.

(2) Develop techniques that enable a layered model to exhibit thin layers without computational failures. Layers with negligible thickness can develop in situations that include coastal upwelling, outcropping of surfaces of constant density to the upper boundary of the fluid due to lateral variations in temperature, or intersections of density surfaces with bottom topography. For the sake of DG computations involving thin layers, this paper develops (i) implementations of wind stress, bottom stress, and interfacial shear stress that do not provoke spuriously large velocities, and (ii) a limiter that maintains nonnegative layer thicknesses in DG solutions.

(3) Test the above techniques in numerical experiments involving model problems.

1. Introduction

This paper describes extensions of previous work by the author to develop procedures for using discontinuous Galerkin (DG) numerical methods in multi-layer models of ocean circulation. Here, the term "multi-layer" means that the vertical coordinate is a quantity related to density; under a straightforward vertical discretization of such a model, the fluid can be approximated as a stack of layers of constant density with thicknesses that can vary with

e-mail: higdon@math.oregonstate.edu (Robert L. Higdon)

position and time. The governing equations for each layer resemble the shallow water equations for a constant-density fluid, with means for communication between layers.

Previous results by the author on this topic are contained in [17] and [18] and are outlined later in this section. For the issues addressed in the present paper, part of the motivation arises from the possibility of layers tending to negligible thickness, although this is not the only motivation. The particular topics addressed here are the following.

- Develop a representation of the horizontal viscosity terms in the momentum equations, in a way that can be used with a DG spatial discretization and a barotropic-baroclinic time splitting. Various splittings of this nature are widely used in ocean modeling to handle efficiently the multiple time scales that can be present in the system. Horizontal viscosity terms are typically included in ocean models in order to parameterize the large-scale effects of unresolvable sub-grid-scale turbulent motions. In the case of a layered model, these terms can also help to suppress erratic velocities that can appear near locations where layer thicknesses approach zero. In the setting of a DG method, viscous terms can be implemented via the "local DG" method, in which the velocity gradient is used in an auxiliary dependent variable that is computed with an additional weak form (Cockburn and Shu [8]). The present paper develops a version of this method for usage in multi-layer ocean models with barotropic-baroclinic splitting.

- Develop implementations of the internal shear stress between fluid layers and the wind and frictional stresses that are applied at the top and bottom of the fluid, respectively. These terms need to be implemented in any case, but particular care should be taken in the case of thin layers.

- In regions where the layer thickness approaches zero, it is possible for the computed thicknesses to become negative in some locations. However, negative thicknesses should be avoided, for reasons that are discussed in Section 3.3. The work in this paper employs a limiter that ensures that all thicknesses are nonnegative everywhere, assuming that the average thickness is nonnegative in each grid cell and in each layer. This limiter is also relevant to the transport of tracers, which are properties or substances that can be carried by a fluid.

Another issue involving DG methods for layered models is the problem of layers interacting with variable bottom topography. However, this topic is beyond the scope of the present paper.

For spatial discretizations in numerical models of ocean circulation, it has been traditional to use finite difference and finite volume methods on logically-rectangular grids. Reviews are given, for example, by Griffies [13] and Higdon [16]. A recent exception to this practice is the usage of finite difference and finite volume methods on variable-resolution Voronoi grids (Ringler et al. [26], Petersen et al. [25]).

Continuous and discontinuous Galerkin methods have been used extensively to solve the two- and three-dimensional shallow water equations for a hydrostatic fluid of constant density. Examples include Bao et al. [4], Bonev et al. [7], Conroy and Kubatko [9], Dawson et al. [10], Giraldo and Warburton [12], Kubatko et al. [20], Wintermeyer et al. [28], Wirasaet et al. [29], and Xing et al. [30]. On the other hand, Pan et al. [24] developed a nonhydrostatic, constant-density coastal model with a DG horizontal discretization and a terrain-fitted vertical coordinate with multiple coordinate surfaces. For the case of variable-density flows, Kärnä et al. [19] developed a hydrostatic coastal ocean circulation model that uses a DG discretization on an unstructured horizontal grid and a terrain-fitted vertical coordinate with a moving vertical mesh.

The present paper, and the previous papers [17] and [18], consider hydrostatic modeling of a variable-density stratified fluid, with a density-based (isopycnic) vertical coordinate and multiple layers. Some advantages of such a vertical coordinate are outlined in Section 2.1. The previous work includes the following.

- ☐ The papers [17] and [18] develop a DG representation of pressure forcing that is valid for an arbitrary vertical coordinate, not just z, and also accounts for discontinuities in layer interfaces across cell edges.

- ☐ The paper [18] develops a version of barotropic-baroclinic time splitting that is suitable for usage with DG spatial discretizations of layered models.

- ☐ An analysis of dispersion relations in [17] shows that DG methods are at least as accurate, and in some cases much more accurate, than some standard finite difference methods for the propagation of linear inertia-gravity waves in a hydrostatic fluid of constant density. This analysis assumes that all quantities are independent of one spatial coordinate, but both components of velocity can be nonzero; the spatial discretization involves a

uniform grid in x, so DG and finite difference methods are equally applicable. The analysis in [17] is supported by numerical experiments involving group velocity and the propagation of wave packets. The later paper [18] includes numerical experiments involving geostrophic adjustment in a multi-layer fluid. During this process, if a fluid is not in geostrophic balance at some location, then inertia-gravity waves radiate away from that location to leave a state that is in balance. A key to the process is the propagation of inertia-gravity waves. Again, the DG method was found to be at least as good as a finite difference method, and in some cases better.

Some widely-quoted advantages of DG spatial discretizations are that they are naturally suited for variable-resolution unstructured meshes and that they allow polynomial approximations of arbitrary degree while maintaining high locality. The latter point enables spatial discretizations of arbitrary order, as measured by local truncation errors and rates of convergence as $\Delta x \to 0$ and $\Delta t \to 0$. These issues are discussed, for example, by Hesthaven [14]. On the other hand, the analysis and computations in [17] and [18] augment this point of view by using wave propagation techniques to determine what can be resolved with fixed values of Δx and Δt. This alternate viewpoint gives another sense in which DG methods can be preferable to some standard finite difference discretizations, in a situation where the two types of methods are equally applicable.

An outline of this paper is the following. Section 2 addresses the choice of vertical coordinate and states the governing equations that are used here. Section 3 discusses the generation of thin layers and some numerical issues that they can cause. Section 4 develops a representation of the horizontal viscosity terms, first without a barotropic-baroclinic splitting and then with such a splitting. Section 5 describes the time-stepping method that is used here. Section 6 discusses the implementation of the shear stress terms, and Section 7 describes a limiter that produces nonnegative values of layer thickness. Numerical computations with some test problems are described in Section 8. One such problem is a purely diffusive problem that tests the implementation of the viscosity terms, and two others are multi-layer fluid problems in which one or more layers can have negligible thickness in some locations. A summary is given in Section 9.

2. Governing equations

This section states pointwise and weak forms of the governing equations that are used throughout this paper. The equations stated below are similar to equations stated in [17] and [18]. However, those papers did not address the implementation of the horizontal viscosity and shear-stress terms, which are included in the present paper, and some broader discussion is given here in order to place those terms in context. This section also includes a brief outline of barotropic-baroclinic splitting.

2.1. The choice of vertical coordinate

A variety of vertical coordinates have been used in numerical models of ocean circulation. Widely-used choices include the elevation z and a terrain-fitted vertical coordinate σ. Another option is an isopycnic coordinate, which is a quantity related to density, such as potential density (density adjusted adiabatically to a pre-determined reference pressure). In the ocean's interior, away from boundary layers, such a quantity is nearly constant along fluid trajectories. In this case, surfaces of constant vertical coordinate are nearly material surfaces, so that a vertical discretization divides the fluid into layers that remain nearly distinct over long times. This property could be an advantage for long-term climate simulations or for tracking the paths of quantities or properties that are transported by the fluid. The present work focuses on isopycnic coordinates, due to these potential advantages.

Another option is a hybrid coordinate, which could be isopycnic in the ocean's interior, z near the top of the fluid, and perhaps σ in near-shore regions (Bleck [5]). This possibility is beyond the scope of the present investigation.

Further discussions of vertical coordinates are contained, for example, in [13], [16], and [22].

2.2. Pointwise form of the governing equations

The paper [16] contains a derivation of the partial differential equations for conservation of mass, momentum, and tracers in a fluid that is in motion relative to a rotating spheroid. In that derivation it is assumed that the vertical length scale is much smaller than the horizontal length scale, for the fluid motions of interest, so that the hydrostatic approximation can be used; that is, vertical accelerations are considered negligible. In the derivation in [16], the vertical coordinate is a generalized coordinate s which is an increasing function of the elevation z at each horizontal

position and time. Otherwise, the coordinate s is arbitrary. The horizontal coordinates are arbitrary orthogonal curvilinear coordinates.

For the discussion in the present paper, assume that the vertical coordinate is isopycnic and that the fluid is approximated as a stack of immiscible layers having constant density. Let the horizontal coordinates be rectangular coordinates x and y, and assume that all quantities are independent of y and that the Coriolis parameter (described below) is nonzero and constant. The y-component of velocity can be nonzero, so the Coriolis effect is present. The assumption of independence on y simplifies the analysis and computations, but it maintains enough complexity to illustrate the issues being addressed here. In this situation, the spatial domain is an interval in x, and if solid-wall boundary conditions are used at the ends of this interval then the governing equations describe flow in an infinite straight channel.

The dependent variables in the governing equations are defined as follows. Number the fluid layers $1, \ldots, R$ from top to bottom; let $p_r(x,t)$ denote the pressure in the fluid at the bottom of layer r at horizontal position x at time t; and let p_0 denote the atmospheric pressure. Then let

$$\Delta p_r(x,t) = p_r(x,t) - p_{r-1}(x,t) \tag{1}$$

denote the vertical pressure difference across layer r, for $1 \le r \le R$. For a diagram of dependent variables, see Fig. 1. Due to the hydrostatic condition, the quantity Δp_r is the weight per unit horizontal area in layer r. That is, Δp_r is g times the mass per unit horizontal area in layer r, where g is the magnitude of the acceleration due to gravity. The quantity Δp_r thus serves as a two-dimensional mass density, times g, for layer r. In a layer of constant three-dimensional density, $\Delta p_r(x,t)$ is proportional to the difference in elevation between the bottom and top of layer r, at (x,t), so Δp_r can also be regarded informally as a layer thickness. The quantity Δp_r serves as the mass variable in the partial differential equations stated below.

Now let $u_r(x,t)$ and $v_r(x,t)$ denote the x- and y-components of velocity, respectively, in layer r at horizontal position x at time t. The quantities $u_r \Delta p_r$ and $v_r \Delta p_r$ are then the components of momentum density (times g) in the x- and y-directions, respectively. They are also components of mass flux, times g.

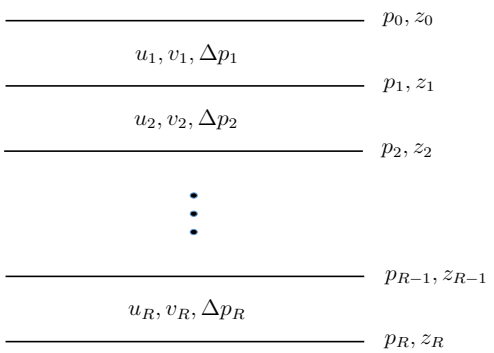

Fig. 1. Diagram of dependent variables. This figure is a schematic representation of a side view of the fluid. The horizontal lines represent interfaces between layers. The layers are numbered $1, \ldots, R$ from top to bottom; $p_r(x,t)$ and $z_r(x,t)$ denote the pressure and elevation, respectively, at the bottom of layer r; $\Delta p_r(x,t) = p_r(x,t) - p_{r-1}(x,t)$ is the vertical pressure increment across layer r; and $u_r(x,t)$ and $v_r(x,t)$ are the x- and y-components of velocity, respectively, in layer r.

Under the present assumptions, the u-component of the momentum equation in layer r is

$$\begin{aligned} \frac{\partial}{\partial t}\left(u_r \Delta p_r\right) + \frac{\partial}{\partial x}\Big[u_r\left(u_r \Delta p_r\right)\Big] - f v_r \Delta p_r \;&=\; -g \int_{z_r(x,t)}^{z_{r-1}(x,t)} \frac{\partial P}{\partial x}(x,z,t)\, dz + g\Big[(\tau_u)_{r-1}(x,t) - (\tau_u)_r(x,t)\Big] \\ &+\; \frac{\partial}{\partial x}\left(A_H \Delta p_r \frac{\partial u_r}{\partial x}\right). \end{aligned} \tag{2}$$

Except for the last term on the right side, this is Eq. (13) in [17]. The last term is the horizontal viscosity term, and it

is included in the more general equations in Section 7.16 of [16]. The viscosity coefficient A_H is assumed here to be a positive constant.

The first term on the right side of (2) is the pressure forcing term; this term is written in a non-standard form and is discussed in Section 2.3. In that term, $z_r(x,t)$ is the elevation of the bottom of layer r. In the second term on the right side, $(\tau_u)_r(x,t)$ is a shear stress at the bottom of layer r; shear stresses are discussed in Section 6. The last term on the left side is the Coriolis term, which accounts for the effects of a rotating coordinate system, and f is the Coriolis parameter. At any location on a rotating spheroid, $f = 2\Omega \sin\theta$, where Ω is the angular rate of rotation of the spheroid and θ is the latitude. However, in the present discussion f is assumed constant.

The v-component of the momentum equation in layer r is

$$\frac{\partial}{\partial t}(v_r \Delta p_r) + \frac{\partial}{\partial x}\Big[u_r (v_r \Delta p_r)\Big] + f u_r \Delta p_r \;=\; g\Big[(\tau_v)_{r-1}(x,t) - (\tau_v)_r(x,t)\Big] + \frac{\partial}{\partial x}\left(A_H \Delta p_r \frac{\partial v_r}{\partial x}\right). \tag{3}$$

Eq. (3) does not contain a pressure forcing term, due to the assumption that all partial derivatives with respect to y are zero. The equation for conservation of mass is

$$\frac{\partial}{\partial t}(\Delta p_r) + \frac{\partial}{\partial x}(u_r \Delta p_r) = 0. \tag{4}$$

2.3. Integral weak forms and horizontal discretization

Next consider the construction of weak forms of the governing equations that can be used to develop discontinuous Galerkin numerical methods.

Let $[a,b]$ be the horizontal spatial interval, and partition $[a,b]$ into grid cells of the form $D_j = [x_{j-1/2}, x_{j+1/2}]$ for $1 \le j \le J$. To obtain a weak form of the u-component (2) of the momentum equation, let ψ be a smooth test function on cell D_j, multiply (2) by $\psi(x)$, and integrate on D_j. The result can be written as

$$\begin{aligned}\int_{D_j} \left\{\frac{\partial}{\partial t}(u_r \Delta p_r) - f v_r \Delta p_r\right\} \psi(x)\, dx \;+\; \Phi_u(j,r,\psi) \;&=\; \Pi_u(j,r,\psi) \;+\; S_u(j,r,\psi) \\ &+ \int_{D_j}\left[\frac{\partial}{\partial x}\left(A_H \Delta p_r \frac{\partial u_r}{\partial x}\right)\right]\psi(x)\, dx\end{aligned} \tag{5}$$

where

$$\Phi_u(j,r,\psi) = \Big[u_r(u_r \Delta p_r)\psi(x)\Big]_{x=x_{j-1/2}}^{x=x_{j+1/2}} - \int_{D_j} u_r(u_r \Delta p_r)\psi'(x)\, dx \tag{6}$$

arises from momentum fluxes,

$$S_u(j,r,\psi) = g\int_{D_j}\Big\{(\tau_u)_{r-1}(x,t) - (\tau_u)_r(x,t)\Big\}\psi(x)\, dx \tag{7}$$

represents shear stresses, and

$$\Pi_u(j,r,\psi) = -g\int_{D_j}\left[\int_{z_r(x,t)}^{z_{r-1}(x,t)} \frac{\partial P}{\partial x}(x,z,t)\, dz\right]\psi(x)\, dx \tag{8}$$

represents the lateral pressure forcing. The last term on the right side of (5) is discussed in Section 4.

The representation (8) of $\Pi_u(j,r,\psi)$ is an integral over the region of fluid in layer r and on cell D_j. In [17] and [18] this integral is transformed by a multi-dimensional integration by parts (i.e., by a Green's identity) to yield a representation involving integrals along the left, right, top, and bottom edges of this fluid region and also on the interior of that region. The latter representation is used to implement the pressure term numerically. This approach is used in order to overcome some difficulties with the lateral pressure forcing that can be encountered when the vertical coordinate is something other than the elevation z; these issues are described in Section 2.4 of [17].

The weak form of the v-component (3) of the momentum equation is similar to (5), except that a pressure term is absent. The weak form of the mass equation (4) is analogous but simpler.

In the case of a discontinuous Galerkin numerical method, each dependent variable in each grid cell at each time level is approximated with a polynomial, with no requirement of continuity across cell edges. Let $\left\{\psi_0^{(j)}, \psi_1^{(j)}, \ldots, \psi_M^{(j)}\right\}$

denote a basis for the space of polynomials used on cell D_j. In [17] and [18] these basis functions are assumed to be Legendre polynomials, with the independent variables scaled and translated to the cell D_j. The basis is then orthogonal on D_j. Represent the momentum densities $u_r\Delta p_r$ and $v_r\Delta p_r$ and the mass variable Δp_r in the form

$$\begin{aligned}(u_r\Delta p_r)(x,t) &= \sum_{n=0}^{M} U_{r,n}^{(j)}(t)\,\psi_n^{(j)}(x)\\ (v_r\Delta p_r)(x,t) &= \sum_{n=0}^{M} V_{r,n}^{(j)}(t)\,\psi_n^{(j)}(x)\\ (\Delta p_r)(x,t) &= \sum_{n=0}^{M} \delta_{r,n}^{(j)}(t)\,\psi_n^{(j)}(x)\end{aligned} \tag{9}$$

for all $x \in D_j$, for all t, and $1 \le r \le R$. For notational simplicity, the equations in (9) make no distinction between the exact values of $u_r\Delta p_r$, $v_r\Delta p_r$, and Δp_r, and their polynomial approximations. The goal of a DG algorithm is to compute the degrees of freedom $U_{r,n}^{(j)}(t)$, $V_{r,n}^{(j)}(t)$, and $\delta_{r,n}^{(j)}(t)$.

To implement the weak form (5) of the u-component of the momentum equation, insert the representation for $u_r\Delta p_r$ in (9) into the first term in (5), and let the test function ψ be each of the basis functions $\psi_0^{(j)}$, $\psi_1^{(j)}$, …, $\psi_M^{(j)}$. The result is a system of $M+1$ ordinary differential equations for the degrees of freedom $U_{r,0}^{(j)}(t)$, …, $U_{r,M}^{(j)}(t)$. The remaining terms in the weak form (5) are regarded as forcing terms, and these need to be evaluated for $\psi = \psi_0^{(j)}, \ldots, \psi_M^{(j)}$ and at each of the time levels and/or stages that are used in the time-stepping method that is used to solve the system of ordinary differential equations.

Section 4 addresses the computation of the last term on the right side of (5), which involves the horizontal viscosity. The shear-stress term $S_u(j,r,\psi)$ is discussed in Section 6. The implementations of the remaining forcing terms in (5) are discussed in [18]. The weak forms of the mass equation and v-component of the momentum equation are implemented in a manner that is analogous to what has just been described.

2.4. Barotropic-baroclinic splitting

The paper [18] develops a barotropic-baroclinic time splitting for DG approximations to the system of governing equations stated above. In general, the solutions of this system can include fast external motions; these motions can be modeled by "barotropic" equations that are obtained by summing, over all layers, the layer equations that are described in Sections 2.2 and 2.3. This vertically-integrated subsystem resembles the shallow water equations for a hydrostatic fluid of constant density. In the present work, this subsystem is solved explicitly with relatively short time steps that are determined by the speed of the fast external gravity waves, which are similar to shallow-water waves.

On the other hand, the equations in the individual layers are solved explicitly with a relatively long time step that is determined by the speeds of slow internal motions. A potential problem is that the layer equations describe the full dynamics of the system and thus admit motions varying on both the fast and the slow time scales, so a violation of the Courant-Friedrichs-Lewy condition seems apparent. However, some procedures described in Section 4.2 of [18] are used to enforce consistency between the layer equations and the vertically-integrated barotropic equations at the end of each long time step. It is shown in [18] that this process provides time filtering that yields a slight modification of the layer equations so that they can be solved successfully with the long time step. These filtered equations are regarded as "baroclinic" (slow) equations. The barotropic and baroclinic equations are solved together with a time-stepping method that involves two baroclinic time levels; this method is described in detail in [18] and is sketched briefly in Section 5.

3. Thin layers

This section describes some ways in which thin layers can be generated, and it also describes some numerical problems that can be caused by such layers.

3.1. Generation of thin layers

One situation in which thin layers can arise is the case of coastal upwelling regions, which are found, for example, off the coast of Oregon. In certain conditions the prevailing wind stress is parallel to the shore, and due to the Coriolis effect the surface waters tend to shift in a direction perpendicular to the wind stress. If that direction is off-shore, then the surface waters are peeled away from the coast, and deeper waters then move up to the surface near the coast. This upwelling contributes to nutrient transport and thus has considerable biological significance. Coastal upwelling regions occupy a relatively small portion of the ocean's surface area but account for a relatively large share of the ocean's biological productivity (Gill [11]). In a vertically-discrete layered model, upwelling can be represented by one or more layers tending to negligible thickness on the affected region.

More generally, thin layers can arise due to lateral variations in density across the global ocean. In particular, the temperatures seen at depth in the tropics may also be seen at the ocean's upper surface at high latitudes. These variations imply that surfaces of constant density within the fluid can outcrop to the upper surface, so that certain layers may not exist physically in certain locations. For example, see Figure 2.1 in [16]. In a numerical model, each layer can be defined to exist at all horizontal positions but could have zero thickness in some regions. Analogous situations arise when surfaces of constant density intersect variable topography at the bottom of the fluid, but that case is not addressed in the present paper.

3.2. Effects of forcing

During the computations described in Sections 8.2 and 8.3, a steady wind stress is applied to the top of a layered fluid that is initially at rest, and after some simulation time the fluid state includes a location where the thickness of the top layer varies rapidly from values near zero to greater values. In some cases, the average thickness of the top layer in one grid cell can be several times greater than the thickness of that same layer in an adjacent cell. Those adjacent cells are subjected to the same wind forcing, and over a given time interval those adjacent cells receive the same impulse and thus the same increment in momentum due to this forcing. However, momentum equals mass times velocity, so the increment in velocity given to the thinner cell is several times greater than the increment in velocity given to the thicker cell. These cell-to-cell contrasts in velocity increments may contribute to the irregular and nonphysical velocity fields that can appear if zero horizontal viscosity is used; these irregular velocities can then lead to irregular mass transport. This problem is addressed by the viscosity term that is developed in Section 4. Some other details related to forcing are discussed in Section 6.1.

3.3. Avoid negative layer thickness

If the thickness of a fluid layer is near zero, then numerical discretization errors could cause the computed values of thickness to become negative in some locations. However, this situation should be avoided. One view of the matter is to consider the shallow water equations for a layer of fluid of constant density. Linearize this system about a state of zero velocity and constant layer thickness. A calculation shows that if this thickness is negative, then the system is not hyperbolic, and the initial value problem is ill-posed.

Another viewpoint is to consider Eq. (4) for conservation of mass. In that equation, the mass flux is $u_r \Delta p_r$. If $\Delta p_r < 0$, then the direction of mass flow is opposite the direction of the velocity, and there are scenarios where a negative thickness could become even more negative. For example, this could occur at the right-most grid cell $[b - \Delta x, b]$ if $u_r > 0$ at $x = b - \Delta x$ but u_r satisfies the solid-wall boundary condition $u_r = 0$ at $x = b$. Such circumstances could lead to numerical instability.

A limiter for avoiding negative layer thickness is described in Section 7.

4. Horizontal viscosity

This section addresses the implementation of the term

$$\int_{D_j} \left[\frac{\partial}{\partial x} \left(A_H \Delta p_r \frac{\partial u_r}{\partial x} \right) \right] \psi(x)\, dx, \tag{10}$$

which is the last term on the right side of the weak form (5) of the u-component of the momentum equation. This term provides part of the forcing for the system of ordinary differential equations discussed in Section 2.3, so this

term is computed at specified times and for arbitrary elements ψ of the basis $\left\{\psi_0^{(j)}, \psi_1^{(j)}, \ldots, \psi_M^{(j)}\right\}$ on grid cell $D_j = [x_{j-1/2}, x_{j+1/2}]$. The corresponding term in the v-component of the momentum equation is similar.

The term (10) needs to be implemented in the context of a barotropic-baroclinic splitting. However, for the sake of clarity we first discuss this term for the case where such a splitting is not used.

4.1. The case where no barotropic-baroclinic splitting is used

An integration by parts shows that the integral (10) is equal to

$$\left[\left(A_H \Delta p_r \frac{\partial u_r}{\partial x}\right)\psi(x)\right]_{x=x_{j-1/2}}^{x=x_{j+1/2}} \quad - \quad \int_{D_j} \left(A_H \Delta p_r \frac{\partial u_r}{\partial x}\right)\psi'(x)\, dx \tag{11}$$

The integral in (11) is computed with a quadrature formula; for the computations described in Section 8, Gauss-Legendre quadrature is used. It is then necessary to obtain values of $\partial u_r/\partial x$ at the quadrature points in each grid cell. In addition, the terms involving $x = x_{j\pm1/2}$ require one-sided limits of $\partial u_r/\partial x$ at those points and a strategy for evaluating these terms at $x_{j\pm1/2}$. It is assumed here that values of ψ, ψ', u_r, and Δp_r are available at all points where those quantities are needed.

The term (11) can be implemented with the "local DG" method (e.g., Cockburn and Shu [8], Arnold et al. [3], Aizinger and Dawson [1], Srinivasan et al. [27]), which employs an auxiliary variable to reduce the order of the derivatives. In the present case, the diffusive flux $A_H(\Delta p_r)\partial u_r/\partial x$ contains a coefficient Δp_r which is a known function of (x, t), whereas in the preceding references the coefficient of the gradient is either a constant or is a function of the dependent variable that is being diffused. For the present case, let

$$q_r(x,t) = \frac{\partial u_r}{\partial x}(x,t) \tag{12}$$

for all $x \in D_j$, for all t, and $1 \le r \le R$. The weak form of Eq. (12) is

$$\int_{D_j} q_r(x,t)\, \psi(x)\, dx \;=\; \int_{D_j} \frac{\partial u_r}{\partial x}\, \psi(x)\, dx \quad = \quad \left[u_r\, \psi(x)\right]_{x=x_{j-1/2}}^{x=x_{j+1/2}} - \int_{D_j} u_r\, \psi'(x)\, dx, \tag{13}$$

and the weak form (10)-(11) of the viscosity term becomes

$$\int_{D_j} \left[\frac{\partial}{\partial x}\Big(A_H\, \Delta p_r\, q_r\Big)\right] \psi(x)\, dx \;=\; \left[A_H(\Delta p_r)\, q_r\, \psi(x)\right]_{x=x_{j-1/2}}^{x=x_{j+1/2}} \;-\; \int_{D_j} A_H(\Delta p_r)\, q_r\, \psi'(x)\, dx \tag{14}$$

As seen in Section 4.1.3, the first weak form (13) is used to obtain pointwise values of q_r at quadrature points and cell edges, and those results are then used to compute (14).

The formulation (12)–(14) differs somewhat from the formulation introduced in [8]. In that reference, the diffusion term has the form $(a(u)u_x)_x$, where u is the dependent variable in an advection-diffusion equation, and $a(u) \ge 0$. Let $b(u) = \sqrt{a(u)}$, and let $g(u)$ be an antiderivative of $b(u)$. The diffusion term is then $(a(u)u_x)_x = (b(u)g'(u)u_x)_x = (b(u)q)_x$, where $q = g(u)_x$. In [8] this representation is used to obtain weak forms corresponding to (13)–(14). An analogue of that approach to the present case is to try $q_r = \sqrt{\Delta p_r}\, \partial u_r/\partial x$. However, this would not have the form $g(u)_x$, and in an analogue of (13) the coefficient $\sqrt{\Delta p_r}$ would be grouped with $\psi(x)$ during the integration by parts. It therefore seemed better to use the approach described above, in (12)–(14).

4.1.1. Values of u_r and q_r at cell edges in the interior of the spatial domain

Before the weak forms (13) and (14) can be used, it is first necessary to specify formulas for u_r and q_r at cell edges. In a DG method these functions can be discontinuous at such points, yet the right sides of (13) and (14) require values of u_r and q_r at $x_{j\pm1/2}$. Values of Δp_r at cell edges are discussed in Section 4.2.4. In (13) and (14), the values of ψ at $x_{j\pm1/2}$ are one-sided limits from within the interior of cell D_j.

For a value of u_r at a cell edge that is interior to the spatial interval $[a, b]$, use an average of one-sided limits,

$$\widehat{u_r} = \Big\{u_r\Big\} \equiv \frac{1}{2}\Big(\, (u_r)_- + (u_r)_+\Big). \tag{15}$$

Here, the subscripts + and − refer to one-sided limits from the positive and negative directions, respectively, at the cell edge. For the sake of simplicity, the notation in (15) does not include an index to specify the edge. For a value of q_r at a cell edge that is interior to $[a, b]$, use

$$\begin{aligned} \widehat{q_r} \;=\; \widehat{\frac{\partial u_r}{\partial x}} \;&=\; \Big\{q_r\Big\} \;+\; C\Big[u_r\Big] \\ &=\; \frac{1}{2}\Big((q_r)_- + (q_r)_+\Big) \;+\; C\Big((u_r)_+ - (u_r)_-\Big). \end{aligned} \tag{16}$$

Here, the square brackets [ ] refer to a jump across the edge, and C is a positive constant. For dimensional consistency, C must have units 1/distance; for the computations described in Section 8, $C = 1/\Delta x$, where Δx is the width of the grid cells.

In the context of elliptic boundary value problems, Arnold et al. [3] tabulate several possibilities for fluxes at cell edges, including various combinations of averages and jumps. This suggests the possibility of using more general formulations than those listed in (15) and (16). However, the formulas given above were found to be effective in the computations described in Section 8.

A motivation for the expression for $\widehat{q_r}$ in (16) is the following. The quantity

$$A_H \Delta p_r \frac{\partial u_r}{\partial x} = A_H (\Delta p_r) q_r$$

in (14) is a diffusive flux that results from spatial variations in u_r. In (16), the terms $(q_r)_-$ and $(q_r)_+$ account for variations of u_r within the grid cells that lie on each side of the cell edge. However, a jump in u_r at the edge is another kind of spatial variation in u_r that gives rise to diffusion, and this possibility is represented by the term $C\Big[u_r\Big]$ in (16). These two separate process are combined in (16). If u_r is continuous at the edge, then (16) reduces to $\widehat{q_r} = \Big((q_r)_- + (q_r)_+\Big)/2$.

4.1.2. Values of u_r and q_r at solid wall boundaries

Next consider the case where a cell edge is an endpoint of the spatial interval $[a, b]$, and assume that this endpoint represents a solid wall. At such a wall, the fluid satisfies the boundary condition $u_r = 0$, which specifies no flow across the boundary. If, in addition, the horizontal viscosity coefficient A_H is positive, then the fluid also satisfies the no-slip boundary condition $v_r = 0$ at that wall.

In the present subsection, the no-normal-flow boundary condition $u_r = 0$ is used to implement the weak forms (13) and (14) for the u-component of the momentum equation. The no-slip condition $v_r = 0$ can be used in an analogous manner to implement the weak forms for the v-component; the details for that case will be omitted here.

First consider the grid cell $D_1 = [x_{1/2}, x_{3/2}] = [a, a+\Delta x]$. At the interior edge $x_{3/2} = a+\Delta x$, use the representations of $\widehat{u_r}$ and $\widehat{q_r}$ in (15) and (16). At the boundary edge $x_{1/2} = a$, let

$$\begin{aligned} \widehat{u_r} \;&=\; 0 \\ \widehat{q_r} \;&=\; (q_r)_+ \;+\; C\Big((u_r)_+ - 0\Big), \end{aligned} \tag{17}$$

where C has the same value as in (16). The zero in the second equation in (17) is included in order to point out explicitly that zero is the target value for u_r at that cell edge.

In the equation for $\widehat{q_r}$ in (17), the term $(q_r)_+$ represents the diffusive effect of spatial variations of u_r within the grid cell D_1, in the limit $x \to a^+$. The term $C\Big((u_r)_+ - 0\Big)$ represents the diffusive effect of any difference between the actual value of $(u_r)_+$ and its target value of zero. This second term is an analogue of Newton's law of cooling, which states that the rate of heat flow in or out of a point mass is proportional to the difference between the temperature of the mass and the temperature of its surroundings.

Now consider the grid cell $D_J = [x_{J-1/2}, x_{J+1/2}] = [b - \Delta x, b]$. At the boundary edge $x_{J+1/2} = b$, use $\widehat{u_r} = 0$ and

$$\widehat{q_r} = (q_r)_- \;+\; C\Big(0 - (u_r)_-\Big). \tag{18}$$

The choice of signs in the second term can be explained by regarding that term as a finite difference approximation to $\partial u_r/\partial x$.

4.1.3. Implementation of the weak forms (13) and (14)

The values of $\widehat{u_r}$ and $\widehat{q_r}$ that are developed in Sections 4.1.1 and 4.1.2 are substituted for u_r and q_r, respectively, in the terms in (13) and (14) that are evaluated at $x_{j\pm 1/2}$. The resulting formulas are the approximations to (13) and (14) that are used in the computational algorithm.

The weak form (13) for q_r is then used as follows. In analogy to (9), let

$$q_r(x,t) = \sum_{n=0}^{M} Q_{r,n}^{(j)}(t)\, \psi_n^{(j)}(x) \tag{19}$$

for all $x \in D_j$, for all t, and $1 \le r \le R$. Insert the representation for q_r in (19) into the left side of (13), and let ψ be each of the basis functions $\psi_0^{(j)}, \psi_1^{(j)}, \ldots, \psi_M^{(j)}$. The result is a set of $M+1$ algebraic equations for the degrees of freedom $Q_{r,0}^{(j)}(t), \ldots, Q_{r,M}^{(j)}(t)$. These degrees of freedom can be used in (19) to compute values of q_r at the quadrature points and endpoints of each grid cell. The values at endpoints are one-sided limits that can be used in the representations of $\widehat{q_r}$ in (16), (17), and (18). The results of these computations are then used to compute the weak form (14) of the viscosity term.

4.2. Viscosity terms with barotropic-baroclinic splitting included

Now extend the preceding ideas to the case where a barotropic-baroclinic time splitting is used to solve the governing equations. A brief outline of barotropic-baroclinic splitting is given in Section 2.4, and further details are given in [18] for the context of a DG spatial discretization.

4.2.1. Splittings of mass and velocity

First consider splittings of the mass and velocity variables for a layered model of the type considered in this paper. Let

$$p_b(x,t) = \sum_{r=1}^{R} \Delta p_r(x,t) \tag{20}$$

for all x in the spatial domain $[a,b]$ and all times t. The quantity p_b is the pressure at the bottom of the fluid minus the atmospheric pressure at the top of the fluid; it is also g times the mass per unit horizontal area for the water column extending from the bottom of the fluid to the top. Now let $p_b'(x)$ denote the value of $p_b(x,t)$ when the fluid is at the global rest state consisting of level interfaces between layers and a level free surface at the top of the fluid, and let $\eta(x,t) = \Big(p_b(x,t) - p_b'(x)\Big)/p_b'(x)$ denote the relative perturbation of p_b from the rest state. Then

$$p_b = (1+\eta)p_b'. \tag{21}$$

Now define $\Delta p_r'$ by the relation

$$\Delta p_r(x,t) = \Big(1+\eta(x,t)\Big)\Delta p_r'(x,t) \tag{22}$$

for $1 \le r \le R$ and all (x,t). Eq. (22) is motivated by the idea that an external motion causes all fluid layers to thicken or thin by approximately the same proportion (e.g., [18]); the factor $1+\eta$ represents the relative thickening or thinning of the layers. The quantity η can vary on the fast external time scale, whereas $\Delta p_r'$ varies mainly on the slow internal time scale. The quantities η and $\Delta p_r'$ are then regarded as barotropic and baroclinic variables, respectively. A comparison of (20), (21), and (22) shows

$$p_b'(x) = \sum_{r=1}^{R} \Delta p_r'(x,t) \tag{23}$$

for all (x,t).

For a splitting of the velocity component u, let

$$\bar{u}(x,t) \;=\; \sum_{r=1}^{R} \frac{\Delta p_r(x,t)}{p_b(x,t)} u_r(x,t) \;=\; \sum_{r=1}^{R} \frac{\Delta p_r'(x,t)}{p_b'(x)} u_r(x,t) \tag{24}$$

denote the mass-weighted vertical average of u over all layers. The quantity $\bar{u}$ is associated with the vertically-integrated barotropic equations, and it can vary on the fast time scale. The residual $u'_r(x,t) = u_r(x,t) - \bar{u}(x,t)$ varies mainly on the slow time scale, and it serves as a baroclinic velocity. The velocity u_r then has the barotropic-baroclinic splitting

$$u_r(x,t) = \bar{u}(x,t) + u'_r(x,t) \tag{25}$$

for $1 \le r \le R$ and all (x,t). The velocity component v can be split in a similar manner.

The preceding splitting of the mass and velocity fields was developed by Bleck and Smith [6]. Note that in these splittings, the prime notation (i.e., $'$) refers to baroclinic variables, not derivatives.

4.2.2. The viscosity term in the layers

The viscosity term (10) includes a factor Δp_r. In order to reduce the complexity of the method that is developed below, this factor is approximated by the slowly-varying baroclinic quantity $\Delta p'_r$, which is defined by the relation $\Delta p_r = (1+\eta)\Delta p'_r$ in (22). The term η is the relative perturbation of p_b from its rest value, so η is approximately the relative perturbation in the height of the entire water column. In the mid-ocean the maximum value of $|\eta|$ is on the order of 10^{-3} or less, so deleting the factor $1+\eta$ has a small effect relative to the uncertainty in the choice of the viscosity coefficient A_H in (10). Some remarks on the values of $\Delta p'_r$ are contained in Section 4.2.4.

The viscosity term to be considered here is then

$$\int_{D_j} \left[\frac{\partial}{\partial x} \left(A_H \Delta p'_r \frac{\partial u_r}{\partial x} \right) \right] \psi(x)\, dx,$$

which can be approximated by

$$\left[A_H(\widehat{\Delta p'_r})\, \widehat{q_r}\, \psi(x) \right]_{x=x_{j-1/2}}^{x=x_{j+1/2}} \; - \; \int_{D_j} A_H(\Delta p'_r)\, q_r\, \frac{d\psi}{dx}\, dx \tag{26}$$

Here, $\widehat{\Delta p'_r}$ and $\widehat{q_r}$ are values of $\Delta p'_r$ and $q_r = \partial u_r/\partial x$, respectively, that are used at the cell edges $x = x_{j\pm 1/2}$.

The quantity q_r can be split as

$$q_r(x,t) = \frac{\partial u_r}{\partial x} \;=\; \frac{\partial \bar{u}}{\partial x} + \frac{\partial u'_r}{\partial x} \;\equiv\; \bar{q}(x,t) + q'_r(x,t) \tag{27}$$

for $1 \le r \le R$ and all (x,t). Here, $\bar{q} = \partial\bar{u}/\partial x$ and $q'_r = \partial u'_r/\partial x$ are the barotropic and baroclinic components, respectively, of q_r. The relation (27) can then be inserted into the integral in (26).

For values of $\widehat{q_r}$ at cell edges that are interior to the spatial domain $[a,b]$, use the representation in (16), as expressed in terms of split variables. A comparison of (16), (25), and (27) shows

$$\begin{aligned} \widehat{q_r} &= \frac{1}{2}\Big((q_r)_- + (q_r)_+ \Big) \;+\; C\Big((u_r)_+ - (u_r)_- \Big) \\ &= \frac{1}{2}\Big((\bar{q})_- + (\bar{q})_+ \Big) + \frac{1}{2}\Big((q'_r)_- + (q'_r)_+ \Big) + C\Big((\bar{u})_+ - (\bar{u})_- \Big) + C\Big((u'_r)_+ - (u'_r)_- \Big) \\ &= \Big\{ \bar{q} \Big\} + C\Big[\bar{u} \Big] + \Big\{ q'_r \Big\} + C\Big[u'_r \Big]. \end{aligned} \tag{28}$$

The quantity $\Big\{ \bar{q} \Big\} + C\Big[\bar{u} \Big]$ is the barotropic contribution to $\widehat{q_r}$, and the quantity $\Big\{ q'_r \Big\} + C\Big[u'_r \Big]$ is the baroclinic contribution.

For values of $\widehat{q_r}$ at solid walls at the endpoints of the spatial domain $[a,b]$, use the conditions (17) and (18), but expressed in terms of the splitting (27), $q_r = \bar{q} + q'_r$. That is, at the boundary edge $x_{1/2} = a$, use

$$\widehat{q_r} \;=\; \Big[(\bar{q})_+ + C(\bar{u})_+ \Big] \;+\; \Big[(q'_r)_+ + C(u'_r)_+ \Big]. \tag{29}$$

At the edge $x_{J+1/2} = b$, use

$$\widehat{q_r} \;=\; \Big[(\bar{q})_- - C(\bar{u})_- \Big] \;+\; \Big[(q'_r)_- - C(u'_r)_- \Big]. \tag{30}$$

In these equations, the barotropic and baroclinic terms are grouped by the brackets.

Pointwise values of $\bar{q} = \partial\bar{u}/\partial x$ and $q'_r = \partial u'_r/\partial x$ can be obtained via the approximate weak forms

$$\begin{aligned}
\int_{D_j} \bar{q}(x,t)\,\psi(x)\,dx &= \left[\widehat{\bar{u}}\,\psi(x)\right]_{x=x_{j-1/2}}^{x=x_{j+1/2}} - \int_{D_j} \bar{u}\,\frac{d\psi}{dx}\,dx \\
\int_{D_j} q'_r(x,t)\,\psi(x)\,dx &= \left[\widehat{u'_r}\,\psi(x)\right]_{x=x_{j-1/2}}^{x=x_{j+1/2}} - \int_{D_j} u'_r\,\frac{d\psi}{dx}\,dx,
\end{aligned} \tag{31}$$

in analogy to the weak form (13) for q_r discussed earlier. For the values of $\widehat{\bar{u}}$ and $\widehat{u'_r}$ at cell edges that are interior to the spatial domain $[a,b]$, use averages of one-sided limits; at solid boundaries, use $\widehat{\bar{u}} = 0$ and $\widehat{u'_r} = 0$. The implementation of the weak forms in (31) is similar to the implementation of (13) that is described in Section 4.1.3.

4.2.3. The viscosity term in the barotropic equations

As noted in Section 2.4, the barotropic equations are obtained by summing, over all layers, the governing equations for each layer. The weak form for the viscosity term in the barotropic system is then obtained by summing the weak form (26) to yield

$$\left[A_H\left(\sum_{r=1}^{R}(\widehat{\Delta p'_r})\,\widehat{q_r}\right)\psi(x)\right]_{x=x_{j-1/2}}^{x=x_{j+1/2}} - \int_{D_j} A_H\left(\sum_{r=1}^{R}(\Delta p'_r)\,q_r\right)\frac{d\psi}{dx}\,dx. \tag{32}$$

For points in the interior of cell D_j,

$$\sum_{r=1}^{R}(\Delta p'_r)\,q_r = \sum_{r=1}^{R}(\Delta p'_r)\,(\bar{q}+q'_r) = \left(\sum_{r=1}^{R}\Delta p'_r\right)\bar{q} + \sum_{r=1}^{R}(\Delta p'_r)q'_r. \tag{33}$$

For cell edges that are interior to the spatial domain $[a,b]$, Eq. (28) implies

$$\sum_{r=1}^{R}(\widehat{\Delta p'_r})\,\widehat{q_r} = \left(\sum_{r=1}^{R}\widehat{\Delta p'_r}\right)\left(\left\{\bar{q}\right\} + C\left[\bar{u}\right]\right) + \sum_{r=1}^{R}(\widehat{\Delta p'_r})\left(\left\{q'_r\right\} + C\left[u'_r\right]\right). \tag{34}$$

The first term on the right side of (34) is a baroclinic quantity times a sum of barotropic quantities, whereas the second term on the right side is purely baroclinic. For cell edges that are located at solid wall boundaries, similar formulas can be obtained by referring to equations (29) and (30).

4.2.4. Values of $\Delta p'_r$

The weak form (26) of the viscosity term contains values of $\Delta p'_r$ in the interior of cell D_j and values of $\widehat{\Delta p'_r}$ at cell edges. Possible choices for the latter include averages of one-sided limits and minima or maxima of such limits. However, in some computations similar to those in Section 8.2, all of those choices for edge values produced irregular values of velocity near locations where a layer thickness tends to zero at the top of the fluid.

The problem is that as the layer thickness tends to zero, the diffusive flux $A_H(\Delta p'_r)\partial u_r/\partial x$ also tends to zero. This is consistent with the fact that the diffusive flux provides forcing to the momentum in layers, and the momentum density also tends to zero as the layer thickness tends to zero. However, wind forcing at the top of the fluid can lead to irregular velocity at the locations in question, as described in Section 3.2, and additional diffusion is needed to control that behavior. For one approach to this problem, let $\Delta\tilde{p}_r(x,t) = \max\left(\Delta p'_r(x,t), \Delta p_{r,min}\right)$ at all quadrature points and endpoints in each grid cell. Here, $\Delta p_{r,min}$ is a pre-determined threshold, and values at endpoints are regarded as one-sided limits. The values of $\Delta\tilde{p}_r(x,t)$ are the same as $\Delta p'_r$, except that they are not allowed to be less than $\Delta p_{r,min}$. Then use the values of $\Delta\tilde{p}_r(x,t)$ as the values of $\Delta p'_r$ in the viscosity term; in the case of cell edges, use averages of one-sided limits of $\Delta\tilde{p}_r$. This method was used in the computations reported in Section 8.

5. Time-stepping

The present section contains some remarks on time-stepping for the coupled barotropic-baroclinic system that has been described in preceding sections. This information is needed for the discussion of interior shear stresses in Section 6.2 and for the description of numerical computations in Section 8.

In principle, any number of time-stepping methods could be tried for this system. The present work uses a two-time-level, predictor-corrector method that was developed in [18] for DG methods and is based on a similar method that was developed in [15] in the context of finite difference spatial discretizations. Let t_n and t_{n+1} be consecutive time levels for the (slow) baroclinic subsystem. First, the barotropic dependent variables are predicted by solving the (fast) barotropic equations over many subintervals of the baroclinic time interval $[t_n, t_{n+1}]$. During this process, the barotropic variables are updated at each substep, whereas all baroclinic quantities in forcing terms are held constant in time, with values taken from time t_n.

Next, the layer equations are used to step the layer variables explicitly from time t_n to time t_{n+1}. During this process, all barotropic quantities in forcing terms are taken to be time averages of values computed over all barotropic substeps of $[t_n, t_{n+1}]$ during the prediction step for the barotropic equations. This averaging is used in order to prevent rapidly-varying motions from being aliased onto the coarse baroclinic time grid. Consistency between the layer equations and barotropic equations is then enforced, as mentioned briefly in Section 2.4.

The barotropic variables are then corrected; in this case, all baroclinic quantities are time averages involving values at time t_n and predicted values for time t_{n+1}. The layer variables are then corrected, with barotropic quantities represented by time averages computed during the barotropic correction. Consistency is again enforced.

A significant issue in the choice of a time-stepping method is the maximum allowable time step, as expressed by the Courant-Friedrichs-Lewy condition. If the two-level method used here is specialized to the case of a single-layer fluid without barotropic-baroclinic splitting, the result is a time-stepping method for the shallow water equations. In [17] this method is included in a stability analysis of several time-stepping methods, as applied to the shallow water equations linearized about a rest state and with piecewise polynomial spatial approximations of degrees 1, 2, and 3. For the case of piecewise quadratic approximations, for example, the stability analysis in [17] shows that for this two-level method the maximum permissible value of the Courant number $c\Delta t/\Delta x$ is approximately 0.16; here c is a wave speed. This bound on the Courant number may seem small, and it is less than the bound for the other time-stepping methods that are discussed in [17], which are Runge-Kutta methods. However, the two-level method uses few operations per time step than the other methods.

For example, two of the methods analyzed in [17] are four-stage Runge-Kutta methods. In the case of piecewise quadratic spatial approximations, the maximum allowable Courant numbers for these two methods are 0.23 and 0.30. These methods use twice as many operations per time step as the two-level method used here, but their maximum allowable time step is not twice as long.

Accuracy is another consideration in the choice of time-stepping method. The earlier paper [17] contains an analysis of dispersion relations for the linearized shallow water equations. Part of this analysis considers DG discretization in space, with solution in time performed either exactly or with the two-level time-stepping method. In each case, with piecewise quadratic spatial approximations, the numerical dispersion relations are nearly identical to the exact dispersion relations for the partial differential equations; see Figs. 3–6 in [17]. In the situation covered by this analysis, the two-level time-stepping method has high accuracy, and this observation is consistent with the results of the numerical experiments reported in [17] and [18]. A comment on spatial accuracy is that if the spatial discretization uses the B-grid or the C-grid finite difference approximations, which are widely used in ocean modeling, then there can be large differences between the exact and numerical dispersion relations, for some ranges of parameters. See Figs. 1–2 in [17].

A final issue is the complexity of implementation. As indicated above, when a barotropic-baroclinic time splitting is used, it is necessary to pass information back and forth between the two subsystems. If a multi-stage Runge-Kutta method is used to solve the layer equations, this communication would be more complicated than with the two-level method, which was designed explicitly for usage with barotropic-baroclinic splitting.

6. Shear stresses

This subsection is concerned with the shear stress term (7), which appears in the weak form (5) of the u-component of the momentum equation in layer r and is repeated here as

$$S_u(j, r, \psi) = g \int_{D_j} \Big\{ (\tau_u)_{r-1}(x, t) - (\tau_u)_r(x, t) \Big\} \psi(x)\, dx. \tag{35}$$

Here, $(\tau_u)_{r-1}$ and $(\tau_u)_r$ are the shear stresses acting on the interfaces at the bottoms of layers $r-1$ and r, respectively. More precisely, these stresses represent the shear force per unit horizontal area exerted by the layer above an interface

on the layer below the interface. An explicit representation (from, e.g., [17]) for a continuously-stratified fluid is

$$\tau_u = \tau_u^{wb} + \rho A_D \frac{\partial u}{\partial z}, \tag{36}$$

where τ_u^{wb} is the sum of the wind stress at the top of the fluid and the frictional stress along the bottom, ρ is the density of the fluid, and A_D is a diapycnal (i.e., across density surfaces) viscosity coefficient. The shear stress in the v-component of the momentum equation is analogous to the above.

The pointwise shear stress term $g\Big[(\tau_u)_{r-1} - (\tau_u)_r\Big]$ is implemented in [15] in the setting of finite difference spatial discretizations. The discussion in the present subsection is an extension of that method to the case of DG spatial discretizations.

6.1. Wind and bottom stresses

The wind stress acts on the upper boundary of the fluid. However, in a multi-layer isopycnic model it would not be good to apply this stress strictly to the upper boundary of the top layer. During one time step on a given grid cell, the wind stress would apply an impulse to the top layer on that cell, and this impulse would represent an increment in momentum in that layer on that cell. Momentum equals mass times velocity, so as the thickness tends to zero, the imparted velocity increases without bound. This situation can then lead to computational failure.

Instead, in a numerical implementation it is useful to represent the wind stress as decaying linearly down to zero over a prescribed vertical distance (Bleck and Smith [6]); for the computations described in Sections 8.2 and 8.3, this distance is assigned to be one meter. With this formulation, if a layer at the top of the fluid has thickness less than this prescribed value, then it receives only a portion of the applied wind stress. As the thickness of such a layer tends to zero, the net wind forcing on that layer also tends to zero; this is in keeping with the fact that the shear stress term provides forcing to the momentum density, which also tends to zero as the layer thickness tends to zero. If, on a given grid cell, the top layer is sufficiently thin but the layer below it has sufficient mass, then the top layer is essentially inactive in that cell and the wind stress is instead applied to the active layer below it.

In general, the preceding technique is not a remedy for the problem mentioned in Section 3.2, which involves thicknesses of the top layer varying rapidly from values near zero to greater values. That case can include thicknesses that are greater than the prescribed vertical distance that is discussed in the preceding paragraph.

The stress at the bottom of the fluid can be parameterized as $\rho c_D |\mathbf{u}_{bot}| \mathbf{u}_{bot}$ (see [6]), where $\mathbf{u}_{bot} = (u_{bot}, v_{bot})$ is the horizontal velocity at the bottom of the fluid and c_D is a dimensionless drag coefficient. This formulation follows the sign convention that the stress is the shear force per horizontal unit area exerted by an upper region on a lower region; the drag exerted on the bottom of the fluid is then $-\rho c_D |\mathbf{u}_{bot}| \mathbf{u}_{bot}$. Like the wind stress, the bottom stress can be implemented as decaying linearly to zero over a predetermined vertical distance.

6.2. Stresses within the fluid

The term $\rho A_D \partial u / \partial z$ in the stress (36) represents the effect of vertical variations of horizontal velocity within the fluid. Given pointwise values of u, this term can be approximated by finite differences in the vertical direction. However, for a model that employs a stack of layers of constant density, widely-varying layer thicknesses can cause problems with the choice of a vertical increment Δz. For the computations described in Sections 8.2 and 8.3, Δz was assigned the constant value $\sqrt{2A_D/|f|}$, which is the thickness of the Ekman frictional boundary layer (e.g., Gill [11]). Here, f is the Coriolis parameter. The interface friction at the bottom of layer r is then approximated by $\rho A_D (u_r - u_{r+1})/\Delta z$.

A more satisfactory representation of the shear stress might be obtained with a higher-order vertical discretization that employs polynomial representations of the vertical variation of each dependent variable within each coordinate layer. However, this possibility is beyond the scope of the present investigation.

Now consider an algorithm for solving the u-component of the momentum equation in layer r on the (long) baroclinic time interval $[t_n, t_{n+1}] = [t_n, t_n + \Delta t]$. In the equations for the degrees of freedom $U_{r,0}^{(j)}(t), \ldots, U_{r,M}^{(j)}(t)$ for the momentum density $u_r \Delta p_r$ (see Section 2.3), first incorporate all terms except for the shear stress between layers. This remark includes the wind and bottom stresses and a tentative implementation of the Coriolis terms (see below), and it applies both to the prediction step and to the correction step for this momentum equation. Given the resulting values of the degrees of freedom, compute corresponding pointwise values of the quantity $u_r \Delta p_r$ at the quadrature points in each grid cell. Denote such values by $(u_r \Delta p_r)^*$. Then, at each quadrature point, define u_r^{**} by

$$(\Delta p_r)^{n+1} u_r^{**} = (u_r \Delta p_r)^* + g \Delta t \Big[(\tau_u)_{r-1}^{**} - (\tau_u)_r^{**}\Big], \tag{37}$$

where

$$(\tau_u)_r^{**} = \rho A_D \frac{u_r^{**} - u_{r+1}^{**}}{\Delta z} \tag{38}$$

if $1 \le r \le R-1$ and $(\tau_u)_0^{**} = (\tau_u)_R^{**} = 0$. That is, $(\tau_u)^{**} = 0$ at the top and bottom of the fluid, and Eq. (38) holds at each of the interfaces within the fluid. The form of Eq. (37) is motivated by the structure of the continuous momentum equation (2).

Eq. (37) is concerned only with the frictional shear stresses between layers, not the wind or bottom stresses, as the latter have already been implemented by this stage. This equation has the form of a finite difference implementation of the pointwise form of shear stress, but its sole purpose is to obtain values of velocity that can be used to compute the weak form (35). In particular, Eq. (37) is equivalent to

$$(\Delta p_r)^{n+1} u_r^{**} = (u_r \Delta p_r)^* + \frac{\rho g A_D \Delta t}{\Delta z}\left[u_{r-1}^{**} - 2u_r^{**} + u_{r+1}^{**}\right] \tag{39}$$

for $2 \le r \le R-1$,

$$(\Delta p_1)^{n+1} u_1^{**} = (u_1 \Delta p_1)^* + \frac{\rho g A_D \Delta t}{\Delta z}\left[0 - (u_1^{**} - u_2^{**})\right] \tag{40}$$

for the uppermost layer, and

$$(\Delta p_R)^{n+1} u_R^{**} = (u_R \Delta p_R)^* + \frac{\rho g A_D \Delta t}{\Delta z}\left[(u_{R-1}^{**} - u_R^{**}) - 0\right] \tag{41}$$

for the bottom layer. Eqs. (39)–(41) constitute a tridiagonal system of equations for $u_1^{**}, \ldots, u_R^{**}$. This system is solved for each quadrature point in each grid cell. The solutions are used to compute the shear stresses (38) at quadrature points, which are then used to compute the integral weak form (35) of the shear stress term.

This integral weak form is then included in the discrete equations for the degrees of freedom for the momentum density $u_r \Delta p_r$. In the time-stepping method developed in [18], the Coriolis terms are implemented implicitly during the correction step for the layer equations, and during the correction step the final action in the algorithm is to re-do this implicit implementation.

Eq. (39) implies that, as the thickness of layer r tends to zero, $u_r^{**} \to \left(u_{r-1}^{**} + u_{r+1}^{**}\right)/2$ if $2 \le r \le R-1$. If the thickness of the top layer tends to zero, then Eq. (40) implies $u_1^{**} \to u_2^{**}$; if the thickness of the bottom layer tends to zero, then (41) implies $u_R^{**} \to u_{R-1}^{**}$. These properties imply a regularization of the shear stress that inhibits spurious forcing in thin layers.

7. A limiter for layer thickness

With a DG spatial discretization, it is possible for the layer thickness Δp_r to have negative values at some locations, even if the average value of Δp_r is positive in each grid cell. This situation is due to excessive variations in the polynomial approximations to Δp_r, and it is primarily a problem with thin layers.

Section 3.3 gives motivations for preventing negative values of layer thickness during a computation. In particular, if $\Delta p_r < 0$ then the mass flux $u_r \Delta p_r$ has a sign that is opposite the sign of the velocity u_r. This suggests that the computational algorithm should be designed so that all values of Δp_r that affect the mass transport remain nonnegative. The weak form of the mass equation (4) is

$$\int_{D_j} \left\{ \frac{\partial}{\partial t} (\Delta p_r) \right\} \psi(x)\, dx \;+\; \left[(u_r \Delta p_r) \psi(x) \right]_{x=x_{j-1/2}}^{x=x_{j+1/2}} \;-\; \int_{D_j} (u_r \Delta p_r) \psi'(x)\, dx \;=\; 0. \tag{42}$$

The present work then uses the criterion that an algorithm should at least maintain nonnegative values of Δp_r at the endpoints and quadrature points in each grid cell. Towards that goal, the present section develops a limiter on variations in Δp_r. Although this limiter focuses on endpoints and quadrature points, the limiter actually produced positive values everywhere in some computations reported in Sections 8.2 and 8.3.

The main idea of the limiter is the following. Assume that, on a given grid cell and in a given layer at a given time, the mean value of Δp_r is nonnegative. Then, if needed, reduce the variation of Δp_r from its mean so that the values of

the modified Δp_r lie within a specified range, at the endpoints and quadrature points in that cell. The limiting process does not affect cell averages of Δp_r, so it conserves the total mass in each grid cell in each layer.

The idea of reducing the variation from the mean has been used, for example, by Zhang and Shu [31] in the context of scalar nonlinear hyperbolic conservation laws; by Xing et al. [30], Bonev et al. [7], and Wintermeyer et al. [28] with the shallow water equations for a single-layer fluid; and by Srinivasan et al. [27] for scalar convection-diffusion equations. The present work adapts and extends that approach to DG modeling of a multi-layer stratified fluid.

For definiteness, the following analysis assumes that the representation (9) of dependent variables is a modal representation, in which $\psi_n^{(j)}$ is the Legendre polynomial of degree n with independent variable scaled and translated to grid cell D_j. The analysis can also be extended to the case of nodal DG methods, in which the basis functions are Lagrange interpolation polynomials and the degrees of freedom are pointwise values of dependent variables at interpolation points. For the case considered here, the representation of Δp_r is

$$(\Delta p_r)(x,t) = \sum_{n=0}^{M} \delta_{r,n}^{(j)}(t)\, \psi_n^{(j)}(x) \tag{43}$$

for all $x \in D_j$, for all t, and $1 \le r \le R$. Here, $\psi_0^{(j)}(x) = 1$ for all $x \in D_j$, and the set $\left\{\psi_0^{(j)}, \psi_1^{(j)}, \ldots, \psi_M^{(j)}\right\}$ is orthogonal on D_j. Each of the terms in (43) for $1 \le n \le M$ then has integral zero on D_j, and $\delta_{r,0}^{(j)}(t)$ is the mean value of Δp_r on cell D_j at time t. It was assumed above that this mean value is nonnegative.

Let A denote the mean (average) value of Δp_r on cell D_j at time t; for simplicity, the dependence of A on r, j, and t is not included in the notation. Then $A = \delta_{r,0}^{(j)}(t) \ge 0$, and Eq. (43) is equivalent to

$$(\Delta p_r)(x,t) \;=\; A + \sum_{n=1}^{M} \delta_{r,n}^{(j)}(t)\, \psi_n^{(j)}(x). \tag{44}$$

The sum for $1 \le n \le M$ in (44) is the deviation of Δp_r from its mean. The limiter developed here is based on modifications of (44) having the form

$$\widetilde{(\Delta p_r)}(x,t) \;=\; A + \beta\left[\sum_{n=1}^{M} \delta_{r,n}^{(j)}(t)\, \psi_n^{(j)}(x)\right] \;=\; A + \beta\Big[(\Delta p_r)(x,t) - A\Big], \tag{45}$$

where β is a constant that satisfies $0 \le \beta \le 1$. In general, β can depend on r, j and t.

To specify the limiter, let γ_{min} and γ_{max} be constants for which $0 \le \gamma_{min} < 1 < \gamma_{max}$; these constants are chosen by the user. The goal is to find a constant β such that $0 \le \beta \le 1$ and

$$\gamma_{min} A \;\le\; \widetilde{(\Delta p_r)}(x,t) \;\le\; \gamma_{max} A \tag{46}$$

for all endpoints and quadrature points in cell D_j. That is, the modified thickness $\widetilde{(\Delta p_r)}(x,t)$ should be at least some specified fraction of the cell mean and at most some specified multiple of that mean. If possible, use $\beta = 1$; otherwise, choose β as large as possible in order to minimize the modification of the solution. The parameter γ_{max} may be unnecessary, but it is mentioned here as a possibility. The computations reported in Sections 8.2 and 8.3 used the values $\gamma_{min} = 0.2$ and $\gamma_{max} = 2.0$.

The construction of the parameter β given in Section 7.1, for given r, j, and t, is based on the maximum and minimum of Δp_r at the endpoints and quadrature points in cell D_j. If the only goal of the limiting process is to prevent negative values of Δp_r at those points, then it would suffice to use $\gamma_{min} = 0$, along with the minimum of Δp_r at those points. On the other hand, if the goal is to produce nonnegative values of Δp_r everywhere in D_j, then using $\gamma_{min} = 0$ would require that one obtain the minimum of Δp_r over all of D_j. The minimum value at the endpoints and quadrature points is only an approximation to that quantity. Using positive values of γ_{min} could compensate for the error in that approximation and thereby create the possibility of obtaining nonnegative values of Δp_r everywhere. Details will not be pursued here analytically. However, the limiter produced positive values of Δp_r everywhere in the numerical experiments reported in Sections 8.2 and 8.3.

A more general problem in limiting is that of suppressing spurious numerical oscillations, even in situations where the positivity of solutions is not an issue. One such technique begins with representing the solution in each grid cell in terms of a Taylor expansion, re-arranged so that each term of positive degree has mean value zero on that cell. If circumstances warrant, use coefficients between 0 and 1 to reduce the magnitudes of some or all of the terms of

positive degree. Various methods can be used to determine such coefficients, and different terms could be reduced by different amounts. This type of method has been used, for example, by Aizinger et al. [2], Kuzmin [21], and Michoski et al. [23], and it is related to the method used in the present paper. A more general survey of limiting is given in the book by Hesthaven [14].

7.1. The contraction factor β

The factor β in (45) serves to contract the deviation of Δp_r from its mean, when needed. To construct β, let B be the maximum of Δp_r at the endpoints and quadrature points in cell D_j at time t, and let b be the minimum of Δp_r at those points. (The dependence of B and b on r, j and t is omitted from the notation.) The condition (46) is satisfied at all of those points if and only if

$$\begin{aligned} A + \beta\Big[B - A\Big] &\leq \gamma_{max} A \\ \gamma_{min} A &\leq A + \beta\Big[b - A\Big]. \end{aligned}$$

The factor β also satisfies $0 \leq \beta \leq 1$, so the largest value of β that satisfies the necessary constraints is

$$\beta = \min\left\{1, \frac{(\gamma_{max} - 1)A}{B - A}, \frac{(1 - \gamma_{min})A}{A - b}\right\}. \tag{47}$$

7.2. Implementation in a multi-layer model

During the process of solving the equation for conservation of mass on each grid cell and in each layer, the limiter is applied at the end of the process, after the degrees of freedom $\delta^{(j)}_{r,0}, \ldots, \delta^{(j)}_{r,M}$ have been computed and the pointwise values of Δp_r have been computed at the endpoints and quadrature points.

First, the pointwise values of Δp_r are used to compute the parameter β in (45) and (47). The limiter is then applied to the degrees of freedom by replacing $\delta^{(j)}_{r,n}$ with

$$\beta\delta^{(j)}_{r,n} = \delta^{(j)}_{r,n} - (1 - \beta)\delta^{(j)}_{r,n} \tag{48}$$

for $1 \leq n \leq M$; see Eq. (45). Similarly, the limiter is applied to the pointwise values of Δp_r by replacing Δp_r with

$$\widetilde{(\Delta p_r)} \;=\; A + \beta\Big[(\Delta p_r) - A\Big] \;=\; \Delta p_r - (1 - \beta)\Big[(\Delta p_r) - A\Big]. \tag{49}$$

This modification of Δp_r cannot be done in isolation, as it necessarily affects the layers above and/or below layer r. Therefore, the adjustment expressed in (45)–(49) is followed by a compensating adjustment in an adjacent layer. Adjustments are done in two steps; sweep vertically from the bottom layer up to the top layer, in order to remedy any negative thicknesses in thin layers along the bottom, and then sweep from the top downward to the bottom in order to deal with any thin layers at the top. The two sweeps are analogous, so only the upward sweep is described here.

During the upward sweep, subtract $(1 - \beta)\delta^{(j)}_{r,n}$ from the existing degree of freedom $\delta^{(j)}_{r,n}$ for mode n in layer r, and then add that same quantity to $\delta^{(j)}_{r-1,n}$, the degree of freedom for that same mode in the layer immediately above. Similarly, subtract $(1 - \beta)\Big[(\Delta p_r) - A\Big]$ from Δp_r at each endpoint and quadrature point, and add the same amount to Δp_{r-1}, the thickness of the layer immediately above.

The quantity Δp_r is g times the mass per unit horizontal area in layer r. This two-dimensional density function is modified by the adjustment just described. However, the adjustment is conservative, in the following senses:

(i) The sum $\Delta p_r(x, t) + \Delta p_{r-1}(x, t)$ is g times the two-dimensional density for layers r and $r - 1$ combined, at horizontal position x and time t, and this sum is not altered at any of the endpoints or quadrature points of any grid cell.

(ii) The adjustment does not affect the cell average $A = \delta^{(j)}_{r,0}(t) \geq 0$, so the total mass in each layer in each cell is not modified. Instead, the adjustment affects only the shapes of the interfaces between layers.

An adjustment in Δp_r could cause a change in Δp_{r-1} that in turn creates a need to adjust Δp_{r-1}. This adjustment process can then have a ripple effect upward through the water column. However, the adjustments stop when the process reaches a layer that is sufficiently thick.

Statements analogous to (i)–(ii) can also be made about the degrees of freedom $\delta^{(j)}_{r,n}$.

8. Numerical computations

This section describes the results of some numerical computations that test the methods developed in preceding sections. For the numerical algorithms that were used in these computations, the aspects that are not developed in the present paper were described and tested in the earlier papers [17] and [18]. Section 8.1 describes a purely diffusive, idealized test problem that checks the formulation of horizontal viscosity that is developed in Section 4. Sections 8.2 and 8.3 present numerical solutions of problems that involve upwelling, downwelling, and thin layers in multi-layer fluids.

8.1. Pure diffusion

For the present test, assume that a two-layer fluid occupies an infinite straight channel for which y is unbounded and $0 \le x \le L$. At the top of the fluid, apply a constant wind stress in the y-direction. De-activate all other forcing terms in the momentum equations, except for the horizontal viscosity. Also de-activate the mass equation, so that Δp_r never varies in time. Under these assumptions, the v-component (3) of the momentum equation in the top layer reduces to

$$\frac{\partial}{\partial t}(v\Delta p) \;=\; g\tau + \frac{\partial}{\partial x}\left(A_H \Delta p \frac{\partial v}{\partial x}\right). \tag{50}$$

Here, the subscripts that indicate the layer have been deleted; and τ denotes the wind stress, which is independent of (x, y, t). The quantity Δp can vary with x but is independent of t. At the boundaries $x = 0$ and $x = L$, impose the no-slip condition $v = 0$.

Initialize the system to a state of rest, and beginning at time $t = 0$ impose the constant wind stress τ. As $t \to \infty$, the system approaches a steady state for which the friction at the boundaries balances the wind forcing, i.e., the rate of energy loss at the boundaries equals the rate of energy input at the top of the fluid. The steady-state velocity v, which depends only on x, then satisfies the boundary value problem

$$\frac{d}{dx}\left(A_H \Delta p \frac{dv}{cx}\right) \;=\; -g\tau \qquad \text{for } 0 < x < L \tag{51}$$

$$v(0) = v(L) = 0. \tag{52}$$

Now assume that the thickness of the top layer, in terms of linear distance, is $cx + d$, where c and d are constants with $c \ge 0$ and $d > 0$. Then $(\Delta p)(x) = \rho g(cx + d)$ for $0 \le x \le L$, where ρ denotes the density of the fluid in the top layer. A linear variation of Δp is chosen here in anticipation of a configuration that is encountered in Section 8.2. Two integrations of Eq. (51), combined with the boundary conditions (52), yield

$$v(x) = \frac{\tau}{c\rho A_H}\left[L\frac{\log(1 + xc/d)}{\log(1 + Lc/d)} - x\right] \tag{53}$$

if $c > 0$ and

$$v(x) = \frac{\tau}{2d\rho A_H} x(L - x) \tag{54}$$

if $c = 0$.

Computed steady-state solutions can be compared to these analytical solutions in order to test the numerical implementation that has been developed here for the viscosity term. The above problem is not physically realistic, but instead it is used only for test purposes. The algorithms used here employ a barotropic-baroclinic splitting, so the de-activation of terms mentioned above applies both to the barotropic equations and to the baroclinic equations.

For the computations described below, the spatial interval is partitioned into 10 grid cells with length $\Delta x = 10$ km, so $L = 100$ km, or 10^5 meters. The wind stress applied to the top of the fluid is $\tau = 0.01$ N/m^2. The viscosity coefficient is $A_H = 80$ m^2/s, which is the same as is used in Sections 8.2 and 8.3. In each of the configurations described below, the top layer has a mean thickness of 50 meters, and the specific volume (reciprocal of density) of that layer is 0.975×10^{-3} m^3/kg. The bottom layer has mean thickness 450 meters, but that layer is inactive in this test. The baroclinic and barotropic time steps are the same as those used in Sections 8.2 and 8.3. For convenience, the times associated with numerical results are stated in terms of model days instead of the number of steps. In the

DG spatial discretization that is used here, quadratic polynomials are used to approximate v in each grid cell; a brief discussion of polynomial degree is included in Section 8.2.

Fig. 2 shows solutions that are obtained when the thickness of the top layer varies linearly from 20 meters at $x = 0$ to 80 meters at $x = L$. In the upper frame in the figure, the solid curve is a graph of the computed v as a function of x at time $t = 200$ days. The dashed curve is a plot of the steady-state solution (53). These plots of v are not symmetric about the midpoint $x = L/2$, due to the nonsymmetric nature of the quantity Δp that appears in the diffusive flux $A_H(\Delta p)dv/dx$. In the lower frame of Fig. 2, the numerical solution at time $t = 800$ is plotted with a solid curve, and the analytical steady state is plotted with a dashed curve. By this time, the system has nearly reached a steady state, and the two curves are indistinguishable in the present plot. The numerical steady state thus agrees very closely with the analytical steady state. Similar behavior, not illustrated here, is obtained if the top layer has a constant thickness of 50 meters; in that case, the solutions are symmetric about the midpoint $x = L/2$.

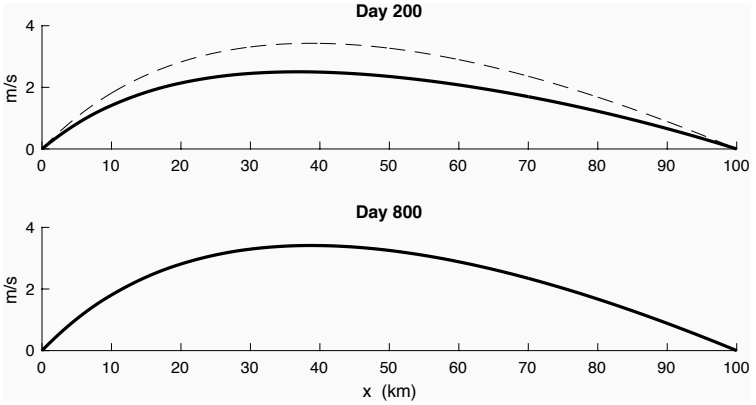

Fig. 2. Plots of v in the purely diffusive test problem, for the case where the thickness of the top layer varies linearly from 20 meters at $x = 0$ to 80 meters at $x = L$. In the upper frame, the solid curve is a graph of the computed v as a function of x at time $t = 200$ days. The dashed curve is a plot of the steady-state solution (53). The lower frame is an analogous plot for model day 800; in this case the two curves are indistinguishable, as the numerical steady state agrees closely with the analytical steady state.

The first paragraph in Section 4.2.2 states that, in the setting of a barotropic-baroclinic splitting, the factor $\Delta p = (1 + \eta)\Delta p'$ in the diffusive flux in the viscosity term can be approximated with the baroclinic quantity $\Delta p'$. For the computation shown in Fig. 2, the quantity η is nonzero, but the approximation $\Delta p \approx \Delta p'$ appears not to degrade significantly the accuracy of the computed solution.

Section 4.2.4 gives a reason for maintaining a minimum value of $\Delta p'$ in the diffusive flux. This stipulation was included in the computations that are described in Sections 8.2 and 8.3, with a value of $\Delta p_{r,min}$ that is equivalent to an elevation difference of 20 meters. If the actual layer thickness is less than that amount, then the modification of $\Delta p'$ in the diffusive flux has the effect of increasing the rate of diffusion. The effect of this procedure is illustrated in Fig. 3. In that figure, the dashed curves show the analytical steady state (53) for the case where the thickness of the top layer varies linearly from 10 meters at $x = 0$ to 90 meters at $x = L$. The solid curves show numerical solutions when the values of $\Delta p'$ in the diffusive flux have a corresponding linear variation, except that a max function is used to prevent $\Delta p'$ from being less than the equivalent of 20 meters. The increased rate of diffusion causes some reduction in the steady-state computed values of v, but the pattern of spatial variation of those values is similar to what is seen in the analytical steady state.

The solutions in Figs. 2 and 3 appear to satisfy the no-slip boundary conditions $v(0) = v(L) = 0$. However, in this DG algorithm these boundary conditions are enforced only weakly, in the sense described in Sections 4.1.2 and 4.2.2. The weak formulation of the viscosity term is used to compute the degrees of freedom for momentum, which are the quantities that are actually computed during the time-stepping for the DG method. Pointwise values of the solution are obtained by combining the degrees of freedom with basis functions, as indicated in the representations (9) of dependent variables. In the case of the numerical steady-state solution illustrated in Fig. 2, for example, the computed boundary values of v are $v(0) \doteq -1.7 \times 10^{-3}$ m/s and $v(L) \doteq 6.5 \times 10^{-5}$ m/s.

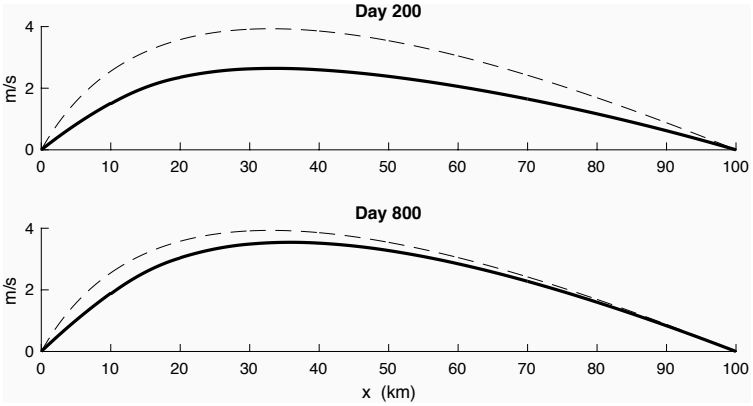

Fig. 3. Plots of v in the purely diffusive test problem, for the case where the thickness of the top layer varies linearly from 10 meters at $x = 0$ to 90 meters at $x = L$. In the numerical experiments described in Sections 8.2 and 8.3 for the multi-layer fluid problem, the values of $\Delta p'$ appearing in the diffusive flux are taken to be no less than the equivalent of 20 meters. The present test illustrates the effect of such a condition. In this case, the restriction on $\Delta p'$ increases the rate of diffusion near the left end of the spatial interval, and this reduces slightly the computed values of v.

8.2. Upwelling, downwelling, and a thin layer in a two-layer fluid

The present subsection describes the results of some numerical computations involving the full algorithm as applied to a fluid with two layers. In this test, a wind stress is applied at the top of the fluid, and this stress generates lateral transport that causes the upper layer to have negligible thickness in some locations. A test with three fluid layers is described in Section 8.3.

For the present test, assume that the fluid occupies an infinite straight channel with vertical sidewalls and a flat bottom. Let x denote a coordinate in the direction across the channel, and let y be a coordinate along the length of the channel. Assume that all quantities in this problem are independent of y.

When the fluid is at the rest state, the upper layer has a uniform thickness of 50 meters, and the lower layer has thickness 450 meters. The specific volumes of the upper and lower layers are 0.975×10^{-3} m^3/kg and 0.970×10^{-3} m^3/kg, respectively. The Coriolis parameter in the momentum equations is $f = 10^{-4}$ s^{-1}, which is similar to the Coriolis parameter on Earth at latitude 45°N. The interval in x is partitioned into 50 grid cells, each with length $\Delta x = 10$ km $= 10^4$ m, so the width of the channel is 500 km.

The horizontal viscosity is $A_H = 80$ m^2/s; some experiments with smaller values of A_H yielded some numerical noise in the velocity field in certain locations. The diapycnal viscosity A_D in the interior shear stress (36) is $A_D = 10^{-4}$ m^2/s. The friction at the bottom of the fluid is represented in the manner described in Section 6.1, with dimensionless drag coefficient $c_D = 0.003$ as used in [6].

The DG spatial discretization uses polynomials of degree two in each grid cell. In the analysis of dispersion relations in [17], which is mentioned in Sections 1 and 5 of the present paper, polynomials of degree two produced results that were noticeably better than polynomials of degree one, but polynomials of degree three yielded diminishing returns. Those results are taken here as a suggestion for the choice of polynomial degree. Polynomials of degree two were also used in the numerical computations described in [17] and [18].

The computations described in the present paper employ the two-level time-stepping method that is outlined in Section 5. The timesteps for this method are determined as follows. A modal analysis similar to the analysis in the Appendix of [18] shows that, for the particular two-layer fluid considered here, the internal and external gravity wave speeds are approximately 1.5 m/s and 70.0 m/s, respectively, for small perturbations of the rest state. However, for the present problem it is assumed that the quantity "c" in the Courant number $c\Delta t/\Delta x$ for the layer equations should be the internal wave speed plus some upper bound on the fluid speed. In the present computations, the timestep Δt_{bcl} for the layer equations, i.e., the baroclinic timestep, is 450 seconds. The bound $c\Delta t/\Delta x < 0.16$ for quadratic spatial discretizations, which is stated in Section 5, is equivalent to $c < 3.56$ m/s when $\Delta x = 10^4$ m. Given that the internal wave speed is approximately 1.5 m/s, this bound allows a fluid speed up to 2 m/s. For the (fast) barotropic equations, there are 23 barotropic substeps per baroclinic step, so the barotropic timestep is $\Delta t_{btp} = 450/23$ seconds. Given that the external wave speed is approximately 70.0 m/s, the Courant number for the barotropic equations is approximately

0.14.

The system is initialized to a state of rest, and beginning at time $t = 0$ a constant wind stress $\tau = 0.1$ N/m^2 is applied at the top of the fluid in the positive y-direction, which is along the length of the channel. The wind stress appears in the v-component (3) of the momentum equation, and it has an immediate effect of inducing positive values of v in the upper layer over the entire spatial interval. The Coriolis term $-fv_r\Delta p_r$ in the u-component (2) of the momentum equation then induces positive values of u in the upper layer.

The effect of this lateral transport in the x-direction (i.e., Ekman transport [11]) is illustrated in Fig. 4. The top frame in the figure shows a cross-section of the fluid at time $t = 50$ days. In this figure, the horizontal coordinate is the cross-channel coordinate x, the vertical coordinate is elevation, and the wind stress at the top of the fluid is directed into the page. During the time interval $0 \le t \le 50$, positive values of u in the upper layer induce a rightward shift of fluid in that layer. At day 50, the upper layer has negligible thickness near the left end of the interval, and at the right end of the interval the upper layer is thicker than at the rest state. Additional lateral transport is seen in the middle frame in Fig. 4, which shows the computed solution at time $t = 100$ days. The bottom frame in that figure shows the computed solution after 600 days. By this time, the system is essentially at a steady state; the computation was executed to time $t = 1000$ days, but plots of the solution after day 600 showed no visible changes relative to day 600. In the steady state, the wind stress at the top of the fluid is balanced by frictional forces along the bottom of the fluid, at the interface between the layers, and at the sidewalls.

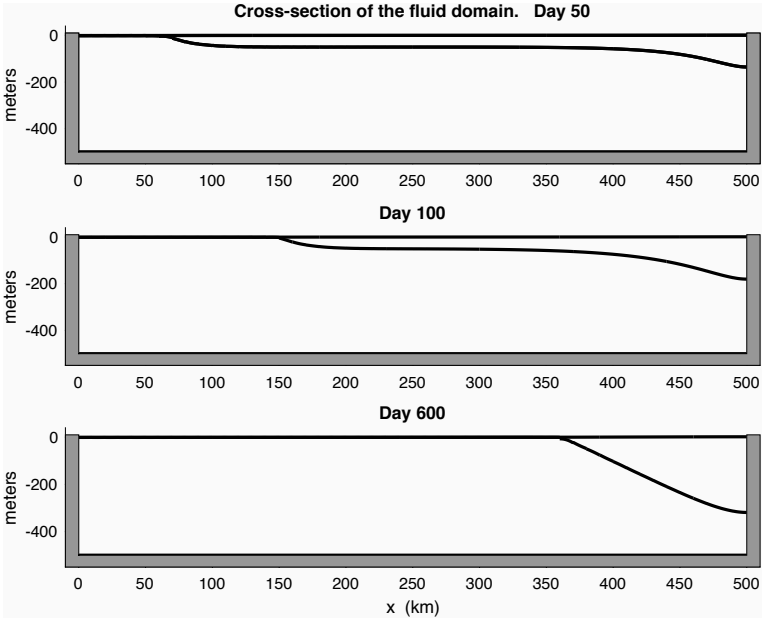

Fig. 4. Cross-sections of a two-layer fluid in an infinite straight channel at model days 50, 100, **and** 600**. Each plot shows the free surface at the top of the fluid and the interface between the two layers. At time** $t = 0$ **the system is at rest, and for that case the free surface and the interface would be represented by straight horizontal line segments. Elevation** $z = 0$ **is the location of the free surface at the rest state. Beginning at time** $t = 0$**, a constant wind stress is applied to the top of fluid along the direction of the channel, which is into the page. Due to the Coriolis effect, the fluid in the upper layer is shifted to the right. Near the left end of the spatial interval, the upper layer is reduced to negligible thickness. By day** 600**, the system is at an approximate steady state. A more detailed view of the free-surface elevation at day** 600 **is given in the bottom frame of Fig. 6.**

In the bottom frame in Fig. 4, the upper layer appears to have negligible thickness on an interval that extends from $x = 0$ to approximately $x = 360$ km. On that interval, the thickness of the upper layer is at most a few tenths of a meter, as illustrated in Fig. 5. The pattern shown in that figure remains stationary after model day 600. In this example, the limiting process described in Section 7 succeeds in maintaining positive layer thicknesses everywhere.

Fig. 6 shows plots of the velocity components v in the upper and lower layers, as functions of x, at time $t = 600$ days. The figure also includes a plot of the elevation of the free surface at the top of the fluid, at that same time.

In the context of plots of cross-sections of the fluid, such as those shown in Fig. 4, positive and negative values of v would represent flow into and out of the page, respectively. Fig. 6 shows that on the portion of the spatial interval

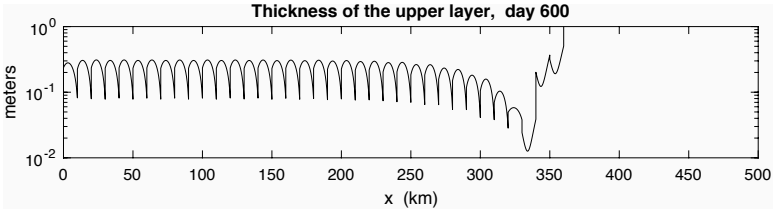

Fig. 5. Thickness of the upper layer in the two-layer fluid at model day 600**. This pattern remains stationary for hundreds of model days. The vertical scale is logarithmic.**

where the upper layer has negligible thickness, the values of v in the upper and lower layers are essentially the same. Elsewhere, the velocity in the upper layer is greater than in the lower layer. In the latter case, for the upper layer the dependence of v on x has an asymmetry that is an analogue of the patterns seen in Figs. 2 and 3, which illustrate the effect of the viscosity term for cases where $\Delta p'$ varies linearly with x except for a requirement that $\Delta p'$ be at least as large as a positive threshold value. A linear variation in the thickness of the upper layer is also seen in the present case, as illustrated on the right end of the bottom frame of Fig. 4.

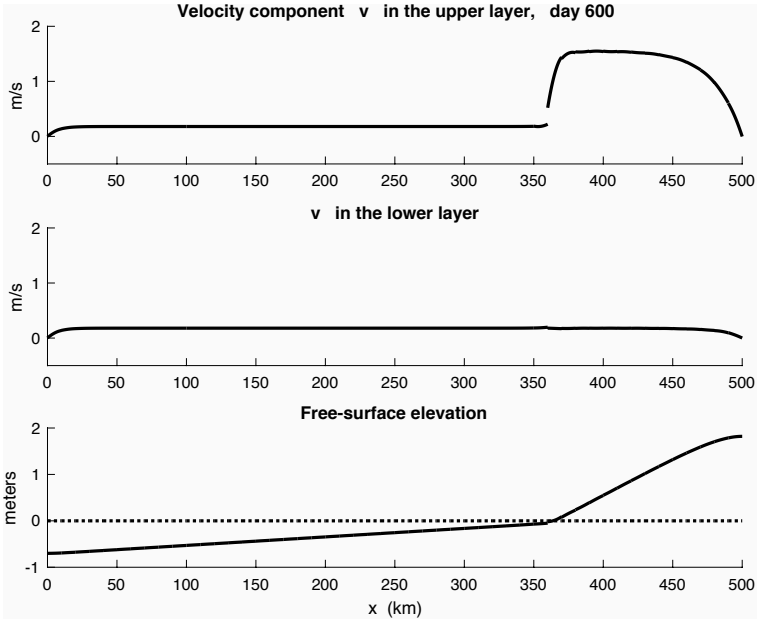

Fig. 6. The top frame shows values of the along-channel velocity v in the upper layer of the two-layer fluid at model day 600**. The middle frame shows v in the lower layer at that same time. In the bottom frame, the solid curve shows the elevation of the free surface at the top of the fluid at day** 600**, and the horizontal dotted line shows the position of the free surface when the fluid is at the rest state. On the interval** $0 < x < 360$ km**, the upper layer has negligible thickness, and the velocities in the two layers are essentially the same. Elsewhere, the upper layer is thicker and can slide over the lower layer. The larger values of v in the upper layer near the right end of the spatial interval imply larger values of the slope of the free surface in that region, due to geostrophic balance in the u-component of the momentum equation.**

The relationships between the computed values of v in the upper and lower layers can be explained as follows. On the interval where the upper layer has negligible thickness, the velocities in the upper and lower layers are locked together, due to the implementation of interfacial shear stress that is described in Section 6.2. In this case, the shear stress at the top of the fluid is balanced by frictional stress along the bottom of the fluid. The bottom stress depends on velocity, so this balance determines v in this region. On the other hand, on the portion of the spatial interval where the upper layer has non-negligible thickness, the velocities in the two layers can differ. In that case, the upper layer can slide over the lower layer, and the wind stress is balanced by the frictional stress between layers, which in turn is balanced by the bottom stress. Details of these processes are described in [15], which develops analytical steady state

solutions for this test problem, in the inviscid case $A_H = 0$.

The analysis in [15] uses the same representations of interfacial stress and bottom stress as in the present paper, with the same values of parameters. In the case where $A_H = 0$, the steady-state value of v in the lower layer is approximately 0.18 m/s, and the steady-state value of v in the upper layer is approximately 1.54 m/s in the region where the upper layer has non-negligible thickness. These values of v are very close to the maximum values of v in the two layers that are attained in the computed solution with $A_H = 80$ m^2/s, as revealed by zoomed-in views (not included here) of plots of the computed solution.

In the plot of the elevation of the free surface that is given in the bottom frame of Fig. 6, the free surface has a greater slope on the region where the upper layer has non-negligible thickness and thus has larger values of v. This situation is a result of geostrophic balance. In the steady state illustrated here, $u = 0$, and the u-component (2) of the momentum equation reduces to a balance between the Coriolis term and the pressure gradient. Larger values of v in the upper layer imply larger values of the Coriolis term and thus larger values of the pressure gradient in that layer; the latter then implies a greater slope of the free surface.

8.3. A three-layer fluid

Next consider a fluid with three layers. For the test computation described here, the layers have specific volumes 0.975×10^{-3} m^3/kg, 0.973×10^{-3} m^3/kg, and 0.970×10^{-3} m^3/kg, ordered from top to bottom. Refer to these layers as layers 1, 2, and 3, respectively. When the fluid is at the rest state, the layers have uniform thicknesses 50 m, 100 m, and 350 m, respectively. All other aspects of the problem are the same as with the two-layer fluid discussed in Section 8.2.

Fig. 7 shows cross-sections of the three-layer fluid at model days 50, 100, and 600. As before, the applied wind stress generates lateral transport that produces thin layers at the top of the fluid near the left end of the spatial interval. By day 50, layer 2 has outcropped to the upper surface of the fluid, and by day 100 layer 3 has also outcropped to the upper surface. By day 600 the interface between layers 2 and 3 has dropped to the bottom of the fluid domain, so that layer 3 has negligible thickness near the right end of the interval. At day 600, the system has not quite reached a steady state.

Fig. 8 shows a plot of the thickness of the top layer at day 600. On the left half of the spatial interval, the top layer has thickness between 10^{-4} and 10^{-3} meters, and on another portion of the interval the top layer has a thickness of a few tenths of a meter. Similar plots of the thicknesses of the other layers (not included here) show that the middle layer has a maximum thickness of about 0.1 meter on the left half of the spatial interval, and the bottom layer has a similar thickness near the right end of the interval. Each of the layers has positive thickness everywhere.

9. Summary

This paper continues a development, begun in [17] and [18], of various procedures that are needed for using discontinuous Galerkin spatial discretizations for multi-layer models of ocean circulation.

One step taken here is to develop an implementation of the horizontal viscosity terms in the momentum equations. This is done by adapting the "local DG" method for usage with barotropic-baroclinic time splitting, a technique that is widely used to deal with the multiple time scales that are present in the system. In general, the local DG method consists of introducing an auxiliary dependent variable q, which is related to the diffusive flux, and then developing a weak Galerkin form for this additional unknown. The additional weak form is used to compute values of q that can then be used in the weak form of the viscosity term. In the implementation developed here, the auxiliary variable for the u-component of the momentum equation is $q = \partial u/\partial x$.

In the setting considered in the present paper, the velocity and mass variables are split into barotropic (rapidly-varying) and baroclinic (slowly-varying) components; the splitting of velocity then induces a splitting of the auxiliary variable q. These split variables appear in the viscosity terms in the layer equations and also in the vertically-integrated barotropic equations that are used to model the fast external motions in the system. The layer equations are solved with relatively long timesteps, and the fast barotropic equations are solved with relatively short substeps. When the layer equations are solved on a long time interval, the barotropic quantities are represented by time averages over all of the substeps of that interval, and in the barotropic part of the algorithm the slow variables are held constant over each of the long time intervals when the barotropic variables are updated with short substeps.

The quantity $q = \partial u/\partial x$ is a factor in the diffusive momentum flux. At the edges of grid cells, this quantity is represented as a combination of two effects: (i) averages of one-sided limits of q from within the interiors of cells,

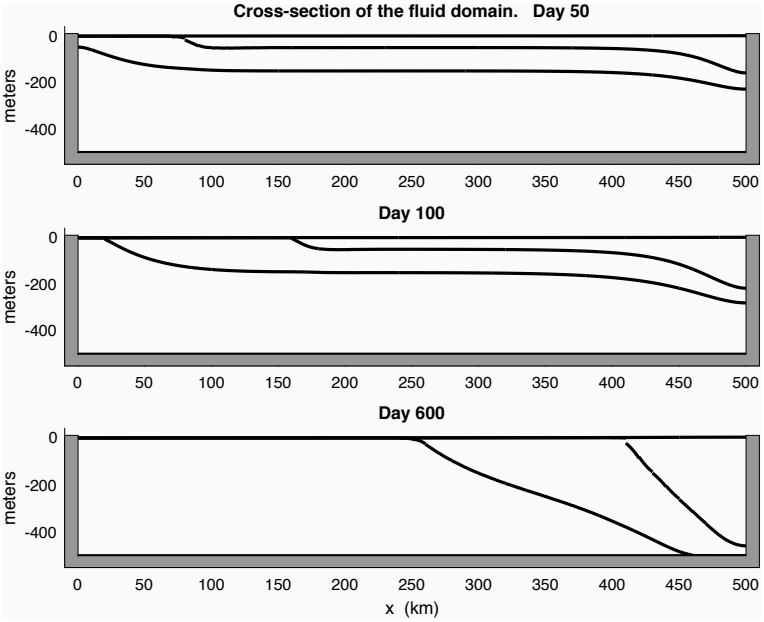

Fig. 7. Cross-sections of a three-layer fluid at model days 50, 100**, and** 600**. Each plot shows the free surface at the top of the fluid and the interfaces between the layers.**

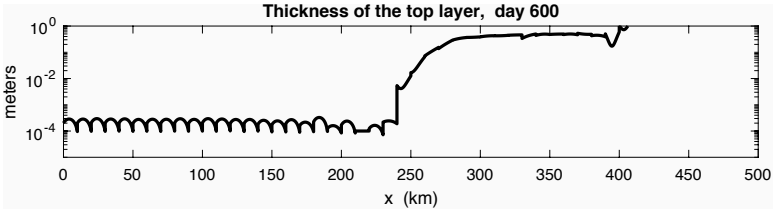

Fig. 8. Thickness of the top layer in the three-layer fluid at model day 600**. The vertical scale is logarithmic.**

in order to represent the diffusive effects of variations of u near the edges, and (ii) terms involving jumps in u at cell edges, which represent diffusive actions across those edges. In the case of a barotropic-baroclinic splitting, these representations at cell edges are split into barotropic and baroclinic components.

This paper also addresses the possibility that thin layers could develop as the state of the fluid evolves. In order to prevent computational failure in this situation, the following steps are taken here.

(i) Shear stresses are implemented so as to inhibit the development of erratic velocities associated with thin layers. In particular, the implementation of the shear stress between fluid layers has a vertically-implicit aspect that regularizes the shear forcing on thin layers. Also, the wind forcing at the top of the fluid is assumed to decay to zero over a short vertical interval instead of being applied strictly to the top layer, which could be arbitrarily thin. A similar process is applied to the frictional stress at the bottom of the fluid.

(ii) In the event that a layer becomes thin in a region, it is possible for the computed layer thickness to become negative in portions of some grid cells, even if the cell averages of thickness remain positive. This would be due to excessive variation in the polynomial approximations to layer thickness. Accordingly, this paper describes a limiter on the variations of such approximations, when such limiting is needed. When this limiter is applied on a given grid cell in a given layer, the deviation of the thickness from the mean is reduced; in the case of a modal DG method this contraction of the deviation is applied both to the degrees of freedom and to the pointwise values of thickness. A compensating adjustment is made in an adjacent layer, either above or below, so that the adjustment only affects the shape of the interface between the two layers. These adjustments are performed in an upward sweep from the bottom of the fluid and a downward sweep from the top. The limiter conserves mass within each layer and in each grid cell.

Numerical computations with model problems are then used to test the methods that are developed here. The first test is a purely diffusive problem that tests the implementation of the viscosity terms. As $t \to \infty$, computed solutions converge to an exact analytical steady state, provided that the same formulas for diffusive flux are used in the numerical and analytical problems. The second test applies the full algorithm to a fluid with two layers. In this case, a wind stress applied at the top of the fluid generates lateral transport that leads to upwelling on one part of the spatial domain and downwelling on another part of the domain. A layer with negligible thickness develops on a part of the domain, and the algorithm successfully maintains nonnegative thickness and prevents the appearance of erratic velocities. In a third test, which uses a fluid with three layers, the algorithm again succeeds in representing layers that develop negligible thickness due to upwelling and downwelling.

References

[1] V. Aizinger, C. Dawson, The local discontinuous Galerkin method for three-dimensional shallow water flow, Comput. Methods Appl. Mech. Engrg. 196 (2007) 734–746.

[2] V. Aizinger, A. Kosík, D. Kuzmin, B. Reuter, Anisotropic slope limiting for discontinuous Galerkin methods, Int. J. Numer. Meth. Fluids 89 (2017) 543–565.

[3] D.N. Arnold, F. Brezzi, B. Cockburn, L.D. Marini, Unified analysis of discontinuous Galerkin methods for elliptic problems, SIAM J. Numer. Anal. 39 (2002) 1749–1779.

[4] L. Bao, R.D. Nair, H.M. Tufo, A mass and momentum flux-form high-order discontinuous Galerkin shallow water model on the cubed-sphere, J. Comput. Phys. 271 (2014) 224–243.

[5] R. Bleck, An oceanic general circulation model framed in hybrid isopycnic-Cartesian coordinates, Ocean Modelling 4 (2002) 55–88.

[6] R. Bleck, L.T. Smith, A wind-driven isopycnic coordinate model of the north and equatorial Atlantic Ocean 1. Model development and supporting experiments, J. Geophysical Research 95C (1990) 3273–3285.

[7] B. Bonev, J.S. Hesthaven, F.X. Giraldo, M.A. Kopera, Discontinuous Galerkin scheme for the spherical shallow water equations with applications to tsunami modeling and prediction, J. Comput. Phys. 362 (2018) 425–448.

[8] B. Cockburn, C.W. Shu, The local discontinuous Galerkin method for time-dependent convection-diffusion systems, SIAM J. Numer. Anal. 35 (1998) 2440–2463.

[9] C.J. Conroy, E.J. Kubatko, *hp* discontinuous Galerkin methods for the vertical extent of the water column in coastal settings part i: Barotropic forcing, J. Comput. Phys. 305 (2016) 1147–1171.

[10] C. Dawson, E.J. Kubatko, J.J. Westerink, C. Trahan, C. Mirabito, C. Michoski, N. Panda, Discontinuous Galerkin methods for modeling hurricane storm surge, Advances in Water Resources 34 (2011) 1165–1176.

[11] A.E. Gill, Atmosphere-Ocean Dynamics, Academic Press, San Diego, 1982.

[12] F.X. Giraldo, T. Warburton, A high-order triangular discontinuous Galerkin oceanic shallow water model, Int. J. Numer. Meth. Fluids 56 (2008) 899–925.

[13] S.M. Griffies, Fundamentals of Ocean Climate Models, Princeton University Press, Princeton, N.J., 2004.

[14] J. Hesthaven, Numerical Methods for Conservation Laws, SIAM, Philadelphia, 2018.

[15] R.L. Higdon, A two-level time-stepping method for layered ocean circulation models, J. Comput. Phys. 177 (2002) 59–94.

[16] R.L. Higdon, Numerical modelling of ocean circulation, Acta Numerica 15 (2006) 385–470.

[17] R.L. Higdon, Pressure forcing and dispersion analysis for discontinuous Galerkin approximations to oceanic fluid flows, J. Comput. Phys. 249 (2013) 36–66.

[18] R.L. Higdon, Multiple time scales and pressure forcing in discontinuous Galerkin approximations to layered ocean models, J. Comput. Phys. 295 (2015) 230–260.

[19] T. Kärnä, V. Legat, E. Deleersnijder, A baroclinic discontinuous Galerkin finite element model for coastal flows, Ocean Modelling 61 (2013) 1–20.

[20] E.J. Kubatko, J.J. Westerink, C. Dawson, hp discontinuous Galerkin methods for advection dominated problems in shallow water flow, Comput. Methods Appl. Mech. Engrg. 196 (2006) 437–451.

[21] D. Kuzmin, A vertex-based hierarchical slope limiter for *p*-adaptive discontinuous Galerkin methods, J. Comput. Appl. Math. 233 (2010) 3077–3085.

[22] F. Lemarié, J. Kurian, A.F. Shchepetkin, M.J. Molemaker, F. Colas, J.C. McWilliams, Are there inescapable issues prohibiting the use of terrain-following coordinates in climate models?, Ocean Modelling 42 (2012) 57–79.

[23] C. Michoski, C. Mirabito, C. Dawson, D. Wirasaet, E. Kubatko, J. Westerink, Adaptive hierarchic transformations for dynamically *p*-enriched slope-limiting over discontinuous Galerkin systems of generalized equations, J. Comput. Phys. 230 (2011) 8028–8056.

[24] W. Pan, S.C. Kramer, M.D. Piggott, Multi-layer non-hydrostatic free surface modelling using the discontinuous Galerkin method, Ocean Modelling 134 (2019) 68–83.

[25] M.R. Petersen, D.W. Jacobsen, T.D. Ringler, M.W. Hecht, M.E. Maltrud, Evaluation of the arbitrary Lagrangian-Eulerian vertical coordinate method in the MPAS-Ocean model, Ocean Modelling 86 (2015) 93–113.

[26] T. Ringler, M. Petersen, R.L. Higdon, D. Jacobsen, P.W. Jones, M. Maltrud, A multi-resolution approach to global ocean modeling, Ocean Modelling 69 (2013) 211–232.

[27] S. Srinivasan, J. Poggie, X. Zhang, A positivity-preserving high order discontinuous Galerkin scheme for convection-diffusion equations, J. Comput. Phys. 366 (2018) 120–143.

[28] N. Wintermeyer, A.R. Winters, G.J. Gassner, T. Warburton, An entropy stable discontinuous Galerkin method for the shallow water equations on curvilinear meshes with wet/dry fronts accelerated by gpus, J. Comput. Phys. 375 (2018) 447–480.

[29] D. Wirasaet, E.J. Kubatko, C.E. Michoski, S. Tanaka, J.J. Westerink, C. Dawson, Discontinuous Galerkin methods with nodal and hybrid

modal/nodal triangular, quadrilateral, and polygonal elements for nonlinear shallow water flow, Comput. Methods Appl. Mech. Engrg. 270 (2014) 113–149.

[30] Y. Xing, X. Zhang, C.W. Shu, Positivity-preserving high order well-balanced discontinuous Galerkin methods for the shallow water equations, Advances in Water Resources 33 (2010) 1476–1493.

[31] X. Zhang, C.W. Shu, On maximum-principle-satisfying high order schemes for scalar conservation laws, J. Comput. Phys. 229 (2010) 3091–3120.